Model Based Detection of Tubular Structures in 3D Images

Karl Krissian, Grégoire Malandain, Nicholas Ayache, Régis Vaillant, Yves Trousset

INSTITUT NATIONAL DE RECHERCHE EN INFORMATIQUE ET EN AUTOMATIQUE

Model Based Detection of Tubular Structures in 3D Images

Karl Krissian — Grégoire Malandain — Nicholas Ayache —

Régis Vaillant — Yves Trousset

N° 3736

July 1999

THÈME 3

apport
de recherche

ISSN 0249-6399

Model Based Detection of Tubular Structures in 3D Images

Karl Krissian , Grégoire Malandain , Nicholas Ayache ,
Régis Vaillant , Yves Trousset

Thème 3 — Interaction homme-machine,
images, données, connaissances
Projet Epidaure

Rapport de recherche n° 3736 — July 1999 — 44 pages

Abstract: Detection of tubular structures in 3D images is an important issue for vascular medical imaging. We present in this report an extension of a previous work done by the same authors [KMA98]. The following improvements have been done:

- a better state of the art,
- a modification of the response function by introducing a coefficient θ whose value is deduced from the model,
- an experimental study on synthetic images with junctions, tangent structures, structures with varying diameters, and tubular structures with Gaussian-like cross-sections or "convolved bar-like" cross-sections,
- an experimental study on a phantom image and on real X-ray and MRA images.

Key-words: filtering, vessel detection, multiscale analysis, segmentation

Unité de recherche INRIA Sophia Antipolis
2004, route des Lucioles, B.P. 93, 06902 Sophia Antipolis Cedex (France)
Téléphone : 04 92 38 77 77 - International : +33 4 92 38 77 77 —Fax : 04 92 38 77 65 - International : +33 4 92 38 77 65

Modélisation et détection de structures tubulaires dans des images 3D

Résumé : La détection des structures tubulaires dans les images tridimensionnelles est une tâche importante pour l'imagerie médicale vasculaire. Ce rapport est une extension d'un travail précédent par les mêmes auteurs [KMA98]. Les modifications et les améliorations suivantes ont été réalisées:

- un état de l'art plus détaillé,
- une modification de la fonction de réponse par l'introduction d'un coefficient θ qui est choisi en fonction du modèle,
- une étude expérimentale sur des images synthétiques contenant des jonctions, des structures tangentes, des structures de diamètre non constant, des structures tubulaires de section gaussienne ou "bar-convoluée",
- une étude expérimentale sur une image de fantôme et sur des images réelles obtenues par rayons X ou par résonance magnétique.

Mots-clés : filtrage, détection de vaisseaux, analyse multi-échelle, segmentation

1 Introduction

1.1 Motivation

In this paper, we present a new method for segmentation and detection of tubular structures in 3D images. Although the proposed method can be applied to any kind of 3D image, it is especially useful for detection of vascular network in medical images. An accurate detection of the vascular network in medical images from various organs (liver, lungs, brain) can help physicians in the planning of surgical operations. Thus, quantification tools are needed because the understanding of 3D images is difficult and visualization tools are not always sufficient to provide the necessary information. Those quantification tools can be obtained by detection of vessels centerlines and segmentation of vascular networks.

1.2 Previous work

A challenge in processing of vascular images is to detect vessels of different sizes. A way to take into account the varying size of vessels in the image is to apply a multiscale analysis. Multiscale analysis allows to detect structures of various sizes according to the scale at which they give a maximal response. We successively present the notions of linear scale-space, of medialness and ridge, and previous work dedicated to vessel detection.

1.2.1 Linear Scale-Space

When applying a multiscale analysis to an image, the use of the convolution product with a Gaussian kernel and its linear partial derivatives has been shown to be the only way to ensure the following properties: linearity, invariance under translation (spatial shift invariance), invariance under rotation (isotropy), and invariance under rescaling [Koe84, Lin94, FtHRKM92]. Florack et al. [FtHRKM92] show that the evolution through scales can be written using two dimensionless variables L/L_0 and x/σ by the means of the Pi-theorem which states that *a function that relates physical observables must be independent of the choice of dimensional units.* σ denotes the standard deviation of the Gaussian kernel, L_0 is the response obtained from the initial image and L is the response obtained at a scale $t = \sigma^2$.

In his works on scale-space theory [Lin94, Lin96], Lindeberg shows the necessity of normalizing the derivatives of the image in the multiscale analysis. He introduces the notion of γ-normalized derivatives:

$$\partial_{x,\gamma-norm} = t^{\gamma} \partial_x \tag{1}$$

When the parameter γ equals one, the normalization ensures invariance under image rescaling, which is compatible with the dimensionless variable $u = x/\sigma$:

$$\frac{\partial I}{\partial u} = \frac{\partial I}{\partial x}\frac{\partial x}{\partial u} = \sigma \frac{\partial I}{\partial x}$$

However, for certain specific task (extraction of 2D blob, of edges, of 2D ridges), Lindeberg studied on analytical models the relationship between the scale at which an object is detected (gives the maximal response), the normalization parameter γ, and the object size, which can lead to choose other values for γ.

In the following, we will implicitly suppose that the scale-space used is linear and obtained from Gaussian convolution of the image and its derivatives.

1.2.2 Medialness

Pizer et al. [PBCF94] uses the notion introduced by Blum [Blu67, BN78] in order to characterize the shape of an object by the means of medial axis containing width information. In 2D images, Blum defined the medial axis as the locus of centers of disks of maximal fit within an object. Making use of the *boundariness* which measures the presence of contours, Pizer et al. define the medial axis, and then the multiscale medial axis (MMA) which defines both the central axis and the width of objects. *Medialness* at a given point and scale $M(x_A, \sigma_A)$ measures the degree of belonging of the point x_A to the medial axis of the object. In [PBCF94], it is defined as the integration over space, scale and direction of a weighted boundariness $W(x_A, x_B, \sigma_A, \sigma_B, u_B)B(x_B, \sigma_B, u_B)$, where the weight W is maximum when: x_B is at a distance from x_A proportional to σ_B with a constant of proportionality k, σ_A is proportional to σ_B with a constant of proportionality c, and u_B has the same orientation and direction as $x_B - x_A$.

In a more recent work [PEFM98], they generalized this notion. The medialness can be defined as a convolution product of the initial image with a kernel $K(x, \sigma)$:

$$M(x, \sigma) = I(x) * K(x, \sigma)$$

To ensure the properties of invariance under rotation, translation, and rescaling, K is based on normalized Gaussian derivatives of intensity, computed at a distance from x proportional to σ and at positions that are rotationally invariant relative to x.

They classify medialness function in two ways: first, central or offset medialness; second, linear or adaptive medialness. On one hand, **central** medialness is obtained by local information, using spatial derivatives of the image at a point x and a scale σ. **Offset** medialness uses the localization of boundaries by averaging spatial information about x over some region whose average radius is proportional to σ. On the other hand, medialness is said to be **linear** when K is radially symmetric and data-independent; and **adaptive** when K is data-dependent.

1.2.3 Ridges of medialness

The different definitions of ridges and their invariance properties were reviewed by Eberly et al. [EGMP94]. They also propose an extension of the concept of ridges of dimension d in n-dimensional images:

If $I(\bar{x})$ is a real-valued function defined for $\bar{x} \in \mathcal{R}^n$, and $H(\bar{x})$ is the Hessian matrix of I at $\bar{x}$.

Assume that the eigenvalues of $H(\bar{x})$ are ordered as $\lambda_1 \leq \ldots \leq \lambda_n$ with associated eigenvectors $(v_i)_{i\in[1,n]}$, and assume that $1 \leq d \leq n$:

$$\bar{x} \textit{ is a ridge point of type } n-d \textit{ if and only if } [v_1 \ldots v_d]^t \nabla I(\bar{x}) = 0 \textit{ and } \lambda_d < 0.$$

In the context of multiscale analysis, ridges can be extracted in a space including the spatial and scale dimensions. The *Multiscale Medial Axis* [PBCF94, MPL94, FPME94] or also called *core* is an example. Extraction of such ridges requires specific algorithms [Lin96, FEPM95, FP98, PEFM98] as for example the so-called Marching Lines [TG92, TG93] derived from the Marching cubes [LC87] and applied for multiscale crest lines extraction in medical images [Fid97].

1.2.4 Works dedicated to vessel detection

We concentrate here on works using multiscale analysis for vessel detection, especially in 3D, and proposing different response functions (or medialness).

The work of Koller et al. [KGSD95] propose a multiscale response in order to detect linear structures in 2D images. The response function uses eigenvectors of the Hessian matrix of the image to define at each point M an orientation orthogonal noted $\mathcal{D}$ to the axis of a potential vessel that goes through M. From this direction, the two points located at equal distance of M in the direction $\mathcal{D}$ are noted M_1 and M_2. The response at M is defined by the minimum of $\mid \overrightarrow{MM_i}.\nabla I(M_i) \mid / \parallel \overrightarrow{MM_i} \parallel$ for $i \in \{1,2\}$.

The authors put the emphasis on the discrimination between contours and vessels centers. They propose also an extension to 3D, but without recommending a particular response because in this case, there are not two points equidistant to M but a circle.

Following this work, Lorenz et al. [LCBF97] decided to use further information from the Hessian matrix: its eigenvalues. Indeed, after a Taylor expansion to second order of the image intensity (Eq. (2)), the eigenvalues of the Hessian matrix, when the gradient is weak, express the local variation of the intensity in the direction of the associated eigenvectors.

$$I(M + h\vec{v}) = I(M) + h\,\nabla I\,\vec{v} + \frac{h^2}{2}\vec{v}^{\,t}\,H(I)\,\vec{v} + \mathcal{O}(h^3) \tag{2}$$

In this way, for white structures on dark background, a **linear** structure has two negative and high eigenvalues and a third one which is low in absolute value, and a **planar** structure has only one negative and high eigenvalue and two other low eigenvalues. This noting leads them to define a response function which depends on the eigenvalues of the Hessian matrix. However, the authors show only a single result on a three dimensional image which contains only two tubular structures.

A more recent work done by Sato et al. [SNSA98, SNAK97] also proposes to choose a response function based exclusively on the eigenvalues of the Hessian matrix. The choice of the response function which combines the three eigenvalues is heuristic and is based on an experimental study on various cases (curved vessels, junctions of vessels).

The interest of their work is to show that a single method can given results on several modalities: MRA, CT and still describing different anatomical structures: vessels in brain, bronchi or liver. Their approach is to provide a visual help in the interpretation of the image after filtering. However, the images used in their experiments seem to have a higher spatial resolution than usual images used in clinical practice, and their algorithm, which uses very few discrete scales, doesn't detect vessel axes and doesn't seem suitable for an accurate estimation of vessel size. In the same state of mind, Frangi et al. [Fra98] propose another response function by interpreting geometrically the eigenvalues of the Hessian matrix.

Using the classification of Pizer et al. described in section 1.2.2, all those works present different choices of medialness that are *adaptive* because they depend on the Hessian matrix in a non-symmetric way, and are either *central* [LCBF97, SNSA98, Fra98] or *offset* [KGSD95].

1.3 Contributions and organisation of the article

The contributions of this paper, based on previous works [KMAV98a, KMAV98b, KMA98], are twofold. First, we propose a new adaptive medialness measure for detection of tubular structures in 3D images. The adaptive property of the medialness is based on the characteristics of the Hessian matrix of the image, its eigenvectors and eigenvalues. The analytic study of those characteristics on different models of vessels including elliptical cross-sections and vessel axis curvature show that eigenvectors and gradient are more stable than eigenvalues. This leads us to choose an offset rather than central medialness response. Second, we use a simple model of cylindrical vessel with circular Gaussian cross-section to guide our detection. The analytic computation allows a scale-selection in the same way as Lindeberg [Lin96]. We then express the relationship between the parameters γ, the selected scale, and the structure width and choose those parameters according to the model. From this relationship, we make a full reconstruction of the vessels network. Other works do not use an explicit model to derive optimal parameters of their response function.

The first section describes a first cylindrical circular model and two derived models that are curved and with non-circular but elliptical cross-section. Those theoretical models are used to compute eigenvalues and eigenvectors of the Hessian matrix and to interpret their values and their sensitivity with respect to the position of the current point, the image intensity, the radius of the structure, the vessel curvature, and the non-circular cross section. The second section describes the proposed measure of medialness, and the automatic scale-selection based on the cylindrical circular model. It also gives the relationship between the size of the structure and its selected scale. Eventually, it explains the extraction of the local extrema and the reconstruction stages. Experiments and results are detailed in a third section. Synthetic images are used to validate the analytical study and to show the behavior of the algorithm under different kinds of tubular structures. Experiments on a phantom image are done to validate our radius estimation. Applications on real images, that are 3D reconstruction of the brain vessels from 2D X-ray angiographies and a brain MRA, are also presented. The vessel network reconstruction is compared to usual isosurfaces rendering or MIP views.

2 Study of second order derivatives on several models

Following the work of [LCBF97], several articles have been dedicated to the visualization of vessels after a multiscale filtering, whose response is exclusively based on the eigenvalues of the image Hessian matrix [SNAK97]. In order to understand the link between the eigenvalues and the local structure of the image, we evaluate in this section the analytic expression of these eigenvalues for several theoretical models derived from a simple cylindrical circular model. The cross-section in each model is either a circular or an elliptical Gaussian blob. We just present here the results, more details about calculation can be found in [KMA98].

In this section, we use the following notations:
- I_0 is the initial image,
- σ_0 denotes the radius of the initial vessel model which is also the standard deviation of a Gaussian,
- G_σ is a Gaussian function with standard deviation σ,
- H is the Hessian Matrix of the image, H' is a simplified matrix proportional to H,
- $\lambda_1, \lambda_2, \lambda_3$ are eigenvalues of the Hessian matrix with $\mid \lambda_1 \mid \geq \mid \lambda_2 \mid \geq \mid \lambda_3 \mid$,
- $\vec{\mathbf{v}}_1, \vec{\mathbf{v}}_2, \vec{\mathbf{v}}_3$ are the associated eigenvectors.

2.1 First model: Cylindrical circular model with Gaussian cross-section

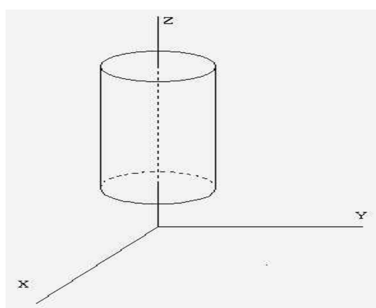

Figure 1: Initial model of a vessel.

The first vessel model that we introduce is cylindrical where (Oz) is the vessel axis and the vessel section is a Gaussian blob:

$$I_0(x,y,z) = C\, G_{\sigma_0}(x,y) = \frac{C}{2\pi{\sigma_0}^2} e^{-\frac{x^2+y^2}{2{\sigma_0}^2}}. \tag{3}$$

where C is a function of σ_0 and $\frac{C}{2\pi{\sigma_0}^2}$ represents the intensity at the center of the vessel (Fig. 1). C depends on the size of the vessel, this dependence is due to partial volume effect that decreases the small vessels intensity.

The model properties are:

- the frontier of the vessel is considered to be at the points where the first derivative in the gradient direction is maximum, i.e., for the points which verify $x^2+y^2={\sigma_0}^2$, thus the vessel radius is σ_0.
- if the model is convolved with a Gaussian kernel of standard deviation σ, the resulting image is another vessel which matches our model but with a radius $\sqrt{\sigma_0^2+\sigma^2}$. This result can be directly deduced from the semi-group property.

In order to better take into account the reality of the vessels, we will study two variations of this model. The first one is a toric circular vessel which allows us to introduce a curvature of the vessel. The second one is a cylindrical vessel with an elliptical cross-section which introduces a variation in the circular shape of the vessel.

2.1.1 Expression of eigenvalues and eigenvectors of the Hessian matrix

The eigenvalues and the eigenvectors of the Hessian matrix H are

$\lambda_3=0$	$\lambda_2=-\frac{I_0}{\sigma_0^2}\left[\frac{\sigma_0^2-(x^2+y^2)}{\sigma_0^2}\right]$	$\lambda_1=-\frac{I_0}{\sigma_0^2}$
$\vec{\mathbf{v}}_\mathbf{3}=(0,0,1)$	$\vec{\mathbf{v}}_\mathbf{2}=(x,y,0)$	$\vec{\mathbf{v}}_\mathbf{1}=(-y,x,0)$

where $I_0=I_0(x,y,z)$ is the initial image, and σ_0 is the radius of the initial image. This means that our model has the following properties:

- Inside the vessel $(x^2+y^2<{\sigma_0}^2)$ we have two negative eigenvalues with eigenvectors in the plane orthogonal to the axis of the vessel.
- The third eigenvalue is null and the associated eigenvector is in the direction of the axis.
- The eigenvalues λ_1 and λ_2 are maxima in absolute value when $x=y=0$ and are equal to $-\frac{I_0(x=0,y=0)}{{\sigma_0}^2}$. λ_2 increases faster than λ_1 as a function of the distance to the center and becomes positive outside the vessel where $\sigma_0^2-(x^2+y^2)$ is negative.

For the multiscale process, the model is convolved with a Gaussian kernel of standard deviation σ and the results are still valid due to the semi-group property but σ_0 has to be replaced by $\sqrt{\sigma_0^2+\sigma^2}$.

2.2 Toric circular model

In this case, the eigenvalues and eigenvectors are similar except that the third eigenvalue is not zero everywhere but only at the center of the vessel (see [KMA98] for more details).

We modelize the vessel with a torus, the big circle parallel to the plane XY and with a radius R and the small circle with a radius equal to r.

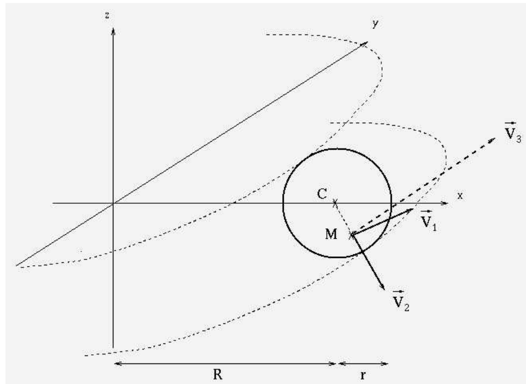

Figure 2: Toric model of a vessel.

The intensity function of the model is given by the expression:

$$I_0(x,y,z) \;=\; Ce^{-\frac{\left(R-\sqrt{x^2+y^2}\right)^2+z^2}{2\sigma_0^2}}.$$

The eigenvectors and eigenvalues of H are (see Fig. 2):

$\lambda_3 = -\frac{I_0}{\sigma_0^2}\left[\frac{x-R}{x}\right]$	$\lambda_2 = -\frac{I_0}{\sigma_0^2}\left[\frac{\sigma_0^2-CM^2}{\sigma_0^2}\right]$	$\lambda_1 = -\frac{I_0}{\sigma_0^2}$
$\vec{\mathbf{v}}_\mathbf{3} = (0,1,0)$	$\vec{\mathbf{v}}_\mathbf{2} = (x-R,0,z)$	$\vec{\mathbf{v}}_\mathbf{1} = (z,0,R-x)$

In order to interpret the value of λ_3 depending on the curvature of the vessel $k = \frac{1}{R}$, we center the reference to the center C of the torus in the plane (Ox,Oy). With the new coordinate $x' = x - R$, we have

$$\lambda_3 \;=\; -\frac{I_0}{\sigma_0^2}\left[\frac{x'}{R+x'}\right] \;=\; -\frac{I_0}{\sigma_0^2}\left[\frac{kx'}{1+kx'}\right].$$

When the curvature is null, $\lambda_3 = 0$ as in the cylindrical case. Nevertheless, this result shows that a vessel curvature can lead to positive ($x > R$) or negative ($x < R$) values of λ_3 in the vicinity of the vessel center. This mean that the absolute value of λ_3 may not be negligible compared to the absolute value of the two other eigenvalues when the vessel curvature is high.

2.3 Cylindrical elliptical model

The elliptical section is defined by one standard deviation along the x axis, σ_x, and one standard deviation along the y axis, σ_y. The model is thus defined by:

$$I_0(x,y,z) \;=\; Ce^{-\frac{1}{2}\left[\left(\frac{x}{\sigma_x}\right)^2+\left(\frac{y}{\sigma_y}\right)^2\right]}.$$

Table 1: sign of the eigenvalues at the point M for the elliptical model.

(1)	$(\frac{x}{\sigma_x})^2 + (\frac{y}{\sigma_y})^2 - 1 < 0$	M is *inside* the ellipse,	$\lambda_1 < 0, \;\; \lambda_2 < 0$
(2)	$(\frac{x}{\sigma_x})^2 + (\frac{y}{\sigma_y})^2 - 1 = 0$	M is *on* the ellipse,	$\lambda_1 < 0, \;\; \lambda_2 = 0$
(3)	$(\frac{x}{\sigma_x})^2 + (\frac{y}{\sigma_y})^2 - 1 > 0$	M is *outside* the ellipse,	$\lambda_1 < 0, \;\; \lambda_2 > 0$

Table 2: Expression of eigenvalues along x and y axis for the elliptical model.

x axis (y = 0)	$\lambda_1 = -\frac{I_0}{\sigma_y^2}\left(1 - \frac{y^2}{\sigma_y^2}\right)$	$\lambda_2 = -\frac{I_0}{\sigma_x^2}$
y axis (x = 0)	$\lambda_1 = -\frac{I_0}{\sigma_y^2}$	$\lambda_2 = -\frac{I_0}{\sigma_x^2}\left(1 - \frac{x^2}{\sigma_x^2}\right)$
center (x = y = 0)	$\lambda_1 = -\frac{I_0}{\sigma_y^2}$	$\lambda_2 = -\frac{I_0}{\sigma_x^2}$

For the sign of the eigenvalues, we can distinguish three cases depending on the position of $M(x, y)$, summarized in table 1. We can also study the eigenvalues along the x and y axis. In both cases, if we choose $\sigma_x > \sigma_y$, $\vec{\mathbf{v}}_\mathbf{1} = (0, 1, 0)$ and $\vec{\mathbf{v}}_\mathbf{2} = (1, 0, 0)$, table 2 gives the analytic expression of the eigenvalues. At the center of the elliptical vessel, one interesting property is that the ratio of the two main eigenvalues is equal to the inverse of the square of the ratio of the respective radii:

$$\frac{\lambda_1}{\lambda_2} = \left(\frac{\sigma_x}{\sigma_y}\right)^2$$

This means that a given variation on the radii ratio will lead to a higher variation of the eigenvalues ratio. (more details can be found in [KMA98]).

2.3.1 Conclusion about the eigenvalues of the Hessian matrix

The three studied models have in common the following properties: at the vessel center one eigenvalue is null with the corresponding eigenvector in the direction of the vessel axis, and the two other eigenvalues are negative and equal if the section is circular, or approximatively equal if the section is an ellipse with $\sigma_x \approx \sigma_y$. The three following conditions express these properties:

$$\frac{-\lambda_1({\sigma_0}^2 + t)}{G_{\sqrt{t}} * I_0} \approx 1 \tag{4}$$

$$\lambda_1 / \lambda_2 \approx 1 \tag{5}$$

$$\mid \lambda_1 \mid \gg \mid \lambda_3 \mid . \tag{6}$$

Eq. (4) comes from the relation $\lambda_1 = -I_0/\sigma_0^2$. It expresses the relationship between the highest negative eigenvalue λ_1, the intensity of the vessel at the current scale $G_{\sqrt{t}} * I_0$, and the vessel radius. At a scale t, ${\sigma_0}^2 + t$ is the square of the vessel radius. However, as the value of σ_0 is not known, this relation is difficult to exploit and the simple criterion $\lambda_2 < 0$ which implies that λ_1 is also negative is used.

Two main difficulties arise for using the previous criteria. The first one is the discrete representation of the image combined with the small size of vessels. Actually, vessels sizes are usually thinner than two or three voxels and the eigenvalues are not computed at the real vessel center but at the center of a voxel. The second one is the non-circular cross-section that increases the uncertainty on criterion (5).

Thus, the vessel models presented in this section emphasize the difficulty in relying on eigenvalues of the Hessian matrix for an accurate detection of vessel center and size. For this reason, we propose to use eigenvalues of the Hessian matrix for the discrimination of vessel-like structures from other structures, and to use a gradient-based response function for the extraction of the vessel centerlines. This extraction is explained in the following section.

3 The method

Our approach can be split into three steps. We first compute the multiscale response from responses at a discrete set of scales, we then extract the local maxima in this multiscale response in order to estimate the vessels centerlines. Vessels are then reconstructed using both the centerlines and the size information. In the first step, we use a model of the vessels both for interpreting the eigenvalues and the eigenvectors of the Hessian matrix and for choosing a good normalization parameter.

Computation of the *single scale response* requires different steps. First, a number of points are pre-selected using the eigenvalues of the Hessian matrix. These points are expected to be near a vessel axis. Then, for each pre-selected point, the response is computed at the current scale. The response function uses information from both eigenvectors of the Hessian matrix and gradient vectors located on a circle centered on the current point. Finally, this response is normalized in order to give a multiscale scale response that combines interesting features of each single scale response. These steps are detailed in the following paragraphs.

The following notations are used:
- t denotes the current scale,
- $M(\bar{x})$ denotes a point in the definition domain of the image I_0, $\bar{x} = (x, y, z) \in \mathcal{R}^3$,
- $R_t(\bar{x})$ is the response for a scale t and at a given location $\bar{x}$,
- R_t^n is the normalized response for a scale t,
- γ is a normalization parameter,
- t_{max} is the scale at which the normalized response is maximal,
- $L(\bar{x}, t) = I_0(\bar{x}) * G_{\sqrt{t}}$ is the image at a scale t.

3.1 Pre-selection of candidates using eigenvalues of the Hessian matrix

In order to compute the response R_t at one scale t, we pre-select points that are expected to be near the vessel axis. This pre-selection is both a discrimination of non-tubular structures and a way to save computation time. In the first section, we studied properties of the eigenvectors and the eigenvalues of the Hessian matrix on different models of vessels. For this pre-selection, we use a weak version of the criteria given in Eq. (4,5,6) where we only test that λ_1 and λ_2 are negative.

3.2 Computation of the response R_t at one scale t

A first choice for R_t can be a 3D extension of the 2D response proposed by Koller et al. [KGSD95]. For a point $\bar{x}$, the response is set to the minimum of the absolute value of the intensity's first order derivative computed at 4 points equidistant from $\bar{x}$. An advantage of this choice is to ensure that a high response results in a high probability of being at a vessel's center, but this medialness response is too sensitive to noise. It seems more natural to use information from the first derivative at every point of a circle than just four points. This circle $C(\bar{x}, \theta\sqrt{t})$ is centered at the current point $\bar{x}$, has a radius $\theta\sqrt{t}$, and is in the plane defined by $\bar{x}$ and the two eigenvectors $\vec{\mathbf{v}}_{\mathbf{1}}$ and $\vec{\mathbf{v}}_{\mathbf{2}}$. The proportionality constant θ will be chosen according to the model. This constant is the inverse of the constant $\rho = \frac{1}{\theta}$ already introduced in [PEFM98]. We will see in section 3.3.3 how this constant can be chosen to optimize the response at the maximal scale.

We propose to use the following medialness response:

$$R_t(\bar{x}) \;=\; \frac{1}{2\pi}\int_{\alpha=0}^{2\pi} -\nabla_t I_0\left(\bar{x} + \theta\sqrt{t}\,\vec{\mathbf{v}}_\alpha\right).\vec{\mathbf{v}}_\alpha d\alpha \tag{7}$$

with $\vec{\mathbf{v}}_\alpha = cos(\alpha)\vec{\mathbf{v}}_{\mathbf{1}} + sin(\alpha)\vec{\mathbf{v}}_{\mathbf{2}}$. This response is the mean of first order derivative information taken at the circle $C(\bar{x}, \theta\sqrt{t})$. $\vec{\mathbf{v}}_\alpha$ is the radial direction and $\nabla_t I_0$ is the gradient vector of the initial image, computed at the scale t. To ensure a positive response for white structure on dark background, we take the opposite of the scalar product between the gradient and the radial direction.

In practice, we must compute this response for a discrete image. Thus, we use $N = E(2\pi\sqrt{t}+1)$ points along the circle $C(M,t)$, where $\forall n \in \mathcal{R}, E(n)$ is the integer part of n, it leads to the discrete formulation:

$$R_t(\bar{x}) \;=\; \frac{1}{N}\sum_{i=0}^{N-1} -\nabla_t I_0\left(\bar{x} + \theta\sqrt{t}\,\vec{\mathbf{v}}_\alpha\right).\vec{\mathbf{v}}_\alpha, \quad \text{with} \;\; \alpha = 2\pi i/N. \tag{8}$$

The value of the gradient vector at the point $\bar{x} + \theta\sqrt{t}\vec{\mathbf{v}}_\alpha$ is obtained by trilinear interpolation of the gradient vector, allowing a better boundary estimation.

3.3 Computation of the multiscale response

3.3.1 Response normalization through scales

One difficulty with multiscale approach is that we want to compare the result of a response function at different scales while the intensity and its derivatives are decreasing functions of scale. Lindeberg [Lin94, Lin96] introduced the notion of normalized derivatives in order to deal with this problem. If the scale t is defined as $t = \sigma^2$ where σ is the standard deviation of the Gaussian, the $\gamma-$**normalized derivative** ∂_γ was already defined by Eq. 1 in section 1.2.1.
At a scale t, the cylindrical circular model with a constant $C > 0$ leads to

$$L(\bar{x}, t) = I_0(\bar{x}) * G_{\sqrt{t}}(\bar{x}) = CG_{\sqrt{\sigma_0^2+t}}(\bar{x}).$$

Appendix A gives some details about the calculation of the maximum of the normalized response R_t^n:

$$R_t^n \ = \ C\frac{\theta t^{\frac{\gamma+1}{2}}}{2\pi\,(t+\sigma_0^2)^2}\, e^{-\frac{\theta^2 t}{2(t+\sigma_0^2)}} \tag{9}$$

We find a relation of proportionality between the scale t_{max} that gives a maximal response and the initial radius of the vessel σ_0:

$$t_{max} \ = \ h(\gamma, \theta)\sigma_0^2 \tag{10}$$

where h is a function of the normalization parameter γ and the proportionality constant θ:

$$h(\gamma, \theta) = \frac{\sqrt{\Delta} - 2\gamma + 2 - \theta^2}{2(3-\gamma)} \quad \text{with} \quad \Delta = \left[\theta^2 - (2\gamma - 2)\right]^2 + 16 - (2\gamma-2)^2 \tag{11}$$

Usually, γ is chosen to allow the response R_t to be maximal for a scale corresponding to the size of the structure we want to detect. To keep generality, we establish the relationship between the scale t_{max} where the maximal response is reached and the initial radius σ_0 of the vessel. This relationship depends on both the normalization parameter γ and the distance coefficient θ. However, this relation still depends on the choice of the structure model, we will see in the experimental study (section 4.1.2) a comparison of this relation between the Gaussian cross-section model and other models.

3.3.2 Zoom-invariant criterion

We define the zoom or rescaling operation of an image as a transformation S with a real positive parameter s and the following property:

$$\forall I \in \mathcal{I},\ \forall (x, y, z) \in D(I),\ \ S(I)(sx, sy, sz) = I(x, y, z).$$

where $\mathcal{I}$ is the set of all images and $D(f)$ is the definition domain of the image I.

A transformation T is zoom-invariant if it commutes with S:

$$\forall I \in \mathcal{I},\ T(S(I)) = S(T(I)) \tag{12}$$

A criterion for normalization is to choose γ in order to ensure a zoom-invariant response function. This choice will avoid privileging vessels of certain radii in the multiscale integration, because the maximal response at the center of a tubular structure will not depend on its size. It will also help to handle interaction between vessels of different sizes. For example, if the maximum response at the center of a big vessel is higher than the maximum response at the center of a small vessel, and the two vessels are neighbours, the big vessel may create side effects which will disturb the extraction of the small vessel in the multiscale integration. Moreover, finding a single threshold to extract the centerlines of all vessels in the final image will be more difficult. Thus, we choose the value 1 for γ. This value is the only one that ensures a zoom-invariant property of our response function as shown in [Lin94].

3.3.3 Choice of the constant θ

The purpose of introducing the parameter θ is to compute the boundariness at a distance which is equal to the frontier of the vessel at the maximal scale t_{max}. This can be achieved for our vessel model. At a given scale t, the frontier of the vessel is at a distance $\sqrt{\sigma_0^2 + t}$ from the vessel center. As the response uses the gradient at a distance $\theta\sqrt{t}$, we would like to have the following relation

$$\theta\sqrt{t_{max}} \;=\; \sqrt{\sigma_0^2 + t_{max}}$$

Introducing Eq. (10) and having set γ to the value 1, we find a solution to this relation given by $\theta = \sqrt{3}$.

Once we have chosen the two parameters γ and θ, two numerical relations can be deduced for our vessel model. The first one is proportional relation between the size of the vessel and the scale at which it is detected $t_{max} = h(\gamma,\theta)\sigma_0^2 = 0.5\ \sigma_0^2$. The second one is the value of the maximal response $R^n_{t_{max}}$:

$$R^n_{t_{max}} \;=\; \left[\frac{C}{2\pi\sigma_0^2}\right] \sigma_0^{\gamma-1} \frac{\theta\, h(\gamma,\theta)^{\frac{\gamma+1}{2}}}{(h(\gamma,\theta)+1)^2}\, e^{-\frac{\theta^2 h(\gamma)}{2(h(\gamma)+1)}} \approx 0.233 \left[\frac{C}{2\pi\sigma_0^2}\right] \tag{13}$$

This value is proportional to the intensity of the vessel center when the background intensity is null. $R^n_{t_{max}}$ is approximatively equal to 0.233 times the intensity at the vessel center $\frac{C}{2\pi\sigma_0^2}$.

3.3.4 Multiscale response

The scales are discretized from t_l to t_h using a logarithmic scale in order to have more precision at low scales.

Fig. 19 shows Maximum Intensity Projections (MIP views) of the normalized responses computed on *image 1* of Fig. 18. Six scales were used for radii of vessels ranging from 1.0 to 3.5: $\{1.0, 1.28, 1.65, 2.12, 2.72, 3.5\}$. If r is the radius of the vessel we want to detect, the associated scale chosen for the detection is $h(\gamma)r^2$.

A MIP view of the initial image is shown at the top left of Fig. 20, and a MIP view of the multiscale response which is the maximum response across the set of scales is shown beside.

3.4 Extraction of local maxima

Our definition of local extrema is a special case of the *Height ridge* definition [FKMP97]. Some recent work [FPE96, Lin96, Fid97] in ridge extraction use the "Marching Lines" algorithm [LC87, TG93].

For each spatial point $M(x, y, z) \in \mathcal{R}^3$, we associate the *scale-space point* $M^t(x, y, z; t) \in \mathcal{R}^3 \times \mathcal{R}_+$. We also define $\vec{\mathbf{t}}$ as a vector in the scale direction.
We define a local maximum in the scale-space normalized response as a point $(\bar{x}; t) \in \mathcal{R}^3 \times \mathcal{R}_+$ which is locally maximal in the directions of $\vec{\mathbf{v}}_1(\bar{x}; t)$, $\vec{\mathbf{v}}_2(\bar{x}; t)$ and $\vec{\mathbf{t}}$. We can easily state that for every central point M of a vessel, its associated scale-space point $M^{t_{max}}$ is locally maximal in the scale-space response. If the converse is true, i.e. all the local maxima in the scale-space response are located at central points of a vessel, then detecting the centerlines is equivalent to extracting those local maxima. This assumption can be verified in the vicinity of the central points. This vicinity is obtained by pre-selection of candidates (paragraph 3.1).

In practice, we use Eq. (14) as a characterization of the local extrema.

$$(\bar{x}; t_i) \text{ is locally maximal} \iff \begin{array}{l} R^n_{t_i}(\bar{x}) \geq R^n_{t_i}(\bar{x} \pm \vec{\mathbf{v}}_1) \text{ and } R^n_{t_i}(\bar{x}) \geq R^n_{t_i}(\bar{x} \pm \vec{\mathbf{v}}_2) \\ \text{and } R^n_{t_i}(\bar{x}) \geq R^n_{t_{i\pm 1}}(\bar{x}) \end{array} \tag{14}$$

Fig. 20 shows at the bottom left a MIP view of the local extrema extracted from the upper left image.

3.5 Reconstruction and visualization

It is not an easy task to visualize the local extrema image in order to improve the interpretation of the original data image. For that purpose, we propose to extract some information from the local extrema image, to superimpose it into some 3D representation of the original data image (volume or surface rendering) or to use it for a vessel network reconstruction.

Line extraction. The image of local maxima contains enhanced information on the vessels centerlines. However, all the extracted maxima are not centers of vessels, some of them with lower intensity value are detected due to noise or to the irregularity of the vessels frontiers. In order to obtain the centerlines from the local maxima image, we *first* binarize the local extrema image by applying a hysteresis thresholding. *Second*, we thin this result to obtain a skeleton-like representation of the vessels. Thinning is achieved by deleting the simple points. These points are the ones whose removal does not change the topology of the image. More details of the skeletonization algorithm can be found in [BM94]. The resulting skeleton is composed of pieces of curves, each of them representing a piece of vessel. *Third*, the skeleton is simplified by removing small pieces of curves. For a better visualization, the remaining curves are smoothed using an energy minimization including data attachment. The smoothing method is derived from [Del94] and doesn't modify the localization of the extremities of each line. The result obtained is an image of the vessel axes.

Reconstruction. The centerline image also contains information about the size of the vessel, which is proportional to the scale at which the current point has been extracted. The relation between a vessel size and the scale at which it was detected was given in paragraph 3.3.2. The bottom right image of Fig. 20 represents a MIP view of the centerlines obtained, where central points are colored according to the scale at which they have been extracted, six colors are used ranging from blue to red for the six single-scale responses shown in Fig. 19.

Each piece of vessel is described by a sequence of points $\{c_i\}$, each of them being associated with an estimated radius r_i. We reconstruct each segment $[c_i, c_{i+1}]$ independently. If the orthogonal projection c of a point M on the line $c_i c_{i+1}$ is into the segment $[c_i, c_{i+1}]$, we estimate the radius in c, and deduce from it the intensity in M with Eq. (3). This way, we reconstruct a grey-level image and we visualize easily all the reconstructed vessels with an isosurface.

Visualization. The usual means of visualizing the vessel network are not effective.

On the one hand, MIP views can mislead the physicians because they don't contain information about the relative position of the vessels in depth. One can add depth-cueing to them but a high intensity vessel located behind a low intensity vessel may still appear to be in front of it, or hide it.

On the other hand, an isosurface of the initial image can account for the the *relative position* of the vessels, but it contains *partial information* about the image which is insufficient. With a low threshold an isosurface contains the small vessels but they are hidden by the big vessels. With a high threshold, it contains only the thickest vessels as shown in Fig. 18.

In both cases, MIP view or isosurface, the superimposition of the detected 3D centerlines can help the interpretation of the real vessel network. Moreover, an isosurface of the reconstructed vessel network have the advantages of an initial image isosurface without having its drawbacks, because all vessels are reconstructed with the same centerline intensity. Thus, it can help to understand the local structure of the vessels network.

4 Experiments and Results

4.1 Experimental study on synthetic images

In this section, we present some experiments made on synthetic images. The purpose is to estimate the sensitivity and to understand the limits of our method on several criteria: normalization, radius estimation, curvature, tangency of vessels, junctions. The created images have a Gaussian blob cross-section and their difference from the theoretical models lies in their discrete representation. This choice allows to check the expected results found by the analytic study. However, we also compare the response profile obtained for *bar-like* and *Gaussian-like* cross-sections on a cylindrical circular model.

This study on synthetic images is not exhaustive, but we hope that it leads to a better understanding of problems arising in vessels segmentation. In the ideal case, the spirit of the work on synthetic images is to *first* find all the difficulties; *second* create synthetic image that isolate each difficulty, understand the behavior of the method on this problem and try to improve it; *third* expect that a single algorithm which handles each of these difficulties separately will give good results on real images.

4.1.1 Cylindrical circular vessels with Gaussian cross-section

Response profile The response profile is the evolution of the medialness response as a function of scale, here taken at the vessel center. Figure 3 shows a comparison between the theoretical and the obtained profiles. The synthetic image contains a circular cylinder with Gaussian blob cross-section, radius 3 voxels and intensity equal to 100 at the center. The theoretical response profile is given by Eq. (9) where $\sigma_0 = 3$, $\gamma = 1$, $\theta = \sqrt{3}$ and $C = 2\pi\sigma_0^2 \times 100$. The experimental response profile is obtained from twenty scales ranging from 0.7 to 3.5. This comparison shows that the two profiles match, and that the experimental profile is slightly lower than the theoretical one near the maximal scale.

Normalization The relationship between the vessel radius and the optimal scale is $t_{max} = h(\gamma, \theta)\sigma_0^2 = 0.5 s_0^2$ where s_0 is the radius of the vessel with Gaussian-like cross-section. The response at the optimal scale and at the vessel center should be zoom invariant and equal to $R^n_{t_{max}}$ times the intensity at the vessel center (see Eq. (13)). The initial image of Fig. 4 contains four vessels with Gaussian blob cross-section and respective radii: 1.25, 1.75, 2.5, 3.5.

After applying the multiscale analysis on this image with 20 scales for vessels radii ranging from 1 to 4 voxels, the second row of Table 3 presents the maximum intensity obtained at the center of each vessel. The difference between the obtained maximal response and the theoretical expected value 23.3 is stronger for small vessels and is probably due to the trilinear interpolation of the gradient vector during the response computation. This difference remains small, below 11%, which confirms the zoom invariant property of the normalization, and will allow an easy threshold of the local extrema image (Fig. 4).

Radius estimation Rows 3 and 5 of Table 3 show radius estimation for the same image. Except for the vessel of size 1.25, the maximum response is obtained at the nearest scale associated to the size of the vessel. The error in size estimation is below 0.3 voxel and improves when the vessel size increases. This result shows that, due to discretization, we cannot hope to get an accurate sub-voxel estimation of the size of small vessels, i.e. vessels of radius below 1.5 voxels.

4.1.2 Other cross-section models

These first tests set the problem of sensitivity to the cross-section model. In real images, there should not be high intensity variations inside the vessel. Two main reasons of intensity variation can be noise and partial volume effect. Concerning noise, the multiscale process that uses Gaussian kernel convolutions tends to reduce it, but depending on the acquisition modality, one can apply a pre-filtering technique like anisotropic diffusion. The partial volume effect disturbs the detection of small vessels and also reduce their intensity. In fact, big vessels can be considered as having a *bar-like* cross-section whereas small one have a *Gaussian-like* cross-section and a lower intensity caused by partial volume effect.

Definition of a bar-like convolved cross-section We are currently working on a vessel model of a bar-like cross-section convolved with Gaussian kernel with a constant and small standard deviation. In this cross-section model, the Gaussian kernel convolution acts like a partial volume effect and can lower the intensity of small vessel: big vessels are *bar-like* and small ones are *Gaussian-like*. Using this kind of model closer to real images, size estimation can be considerably improved.

An analytic expression of the model is given by:

$$I_r(x, y, z) = f_r(x, y) * G_{\sigma_p}(x, y) \tag{15}$$

where r is the radius of the vessel, σ_p is a constant, and f is defined by

$$\begin{aligned} f(x, y) &= 1 \text{ if } \sqrt{x^2 + y^2} \leq r \\ &= 0 \text{ otherwise.} \end{aligned}$$

Comparison of the response profiles Fig. 7 shows response profiles for different cross-sections on a cylindrical circular vessel of radius 3. In red, the profile for a Gaussian-like cross-section, the same as in Fig. 3, and in blue the response profile for a bar-like cross-section. There are important variations between those two profiles, bar-like cross-section have they maximum with a higher response value and at a lower scale. This result shows that our vessel size estimation can not be accurate without having a good model of the vessel cross-section. Fig. 7 shows in green the profile response obtained for a bar-like cross-section of radius three and convolved with a Gaussian kernel of standard deviation 1, and in red the profile using a standard deviation equal to the vessel radius (3).

Radius estimation for the convolved bar-like model Using *Maple*, which is a program for symbolic calculus, and the expressions of our response for the bar-like convolved model given by Eq. 18 in appendix B, we computed the curve that represents the maximal scale $\sigma_{max} = \sqrt{t_{max}}$ as a function of the vessel radius. The result is represented in Fig 8. Although the size estimation requires the use of more complex cross-section models, there is a increasing function s that links the maximal scale and the radius of a vessel. Simulation allows to estimate this function on a bar-like cross-section model convolved with a constant Gaussian. A vessel of a given radius is detected at a lower scale for a bar-like convolved model, thus, for a given maximal scale, the radius of the detected vessel is bigger for a bar-like convolved model than for a Gaussian-like model. Using this simulation, a better radius estimation can be acheived, and this result will be used in the next section on a phantom image.

4.1.3 One vessel with varying width

Fig. 9 and Fig. 10 show experiments made on vessels with varying width. The vessel size of the images is a periodic sinusoid and the radius varies from 2 to 4 voxels with a period of $zsize/n$ voxels $n \in [1, 2, 4]$ and $zsize = 100$, along z axis. The equation of the vessel radius for $n = 1, 2, 4$ is :

$$R(z) = 4 + 2\sin\left(2\pi n \frac{z}{zsize}\right)$$

The local extrema in Fig. 9 shows that the vessel center has been well detected and also that some extrema were detected near the vessel frontiers when the radius goes though a maximum. In this case, there are two negative eigenvalues in the plane tangent to the vessel contour, and it is normal to obtain local extrema. Nevertheless, the response obtained at the vessel center is higher and the *false* responses can be removed either by thresholding of the image of local extrema or by removal of small connected components.

Fig. 10 shows the estimated radius (in red) along z axis compared to the real radius profile of the vessel (in blue). For smooth variations, on the left, the size is well estimated, but for fast variations of radius, on the right, in regions of maximum radius the size is under-estimated due to the Gaussian convolution at high scales that decreases the intensity near those frontiers, faster than in the cylindrical case.

4.1.4 Curved vessels

For a single torus with a Gaussian cross-section, the local extrema gives high response at the torus center where the intensity is higher than 18.00 and some response near the outside frontier of the torus. This second type of response is explained by the negative value of the third eigenvalue that becomes higher in absolute value than the second one (see section 2.2). However, it has an intensity lower than 9.0 and can easily be threshold. Fig. 11 right shows the threshold extrema superimposed on the initial image. The location of the vessel center doesn't have a sub-voxel precision, but the voxels found for the vessel center contain the real vessel center independently of the curvature (bottom row of Fig. 11).

4.1.5 Tangent vessels

We say that two vessels are tangent when their frontiers are enough near to disturb the estimation of the gradient. Generally, the tangency concerns two vessels but in some cases more vessels can be involved, or a vessel can be tangent to a non-vessel structure. We restrict the study to the case of two vessels.

The tangency can be characterize by three parameters: 1) the minimal distance d between the two vessels frontiers compared to the size of the vessels; 2) the ratio between the two vessels radii; 3) the angle $\alpha \in [0, \pi/2]$ between the two vessels axis at the tangent locus.

In our experiments, we set the ratio of the two vessels to 1 (their radius is three voxels) and tested the cases $\alpha = 0$ in Fig. 12 and $\alpha = \pi/2$ in Fig. 13.

Fig. 12 shows results on the first case $\alpha = 0$ where the distance d is equal to zero on the right and to the vessel radius i.e. three voxels on the left. When $d = 0$, a third line is detected between the two vessels and at a higher scale (bottom right), while the continuities of the two vessels centerlines are preserved. As the detected lines are not connected, it is possible to remove the "wrong" line by removing small connected components, but not by thresholding the local extrema image. On the bottom left image, the distance between the two vessels is equal to their radius and a thresholding of the local extrema image is sufficient for removing the "wrong" detected local extrema.

Fig. 13 shows results for $\alpha = \pi/2$, where the distance d decreases from 4 voxels to 0. In this case, there is no third line created by the tangency, but the disturbance on the centerline position is more important. This important displacement of the vessel center for a vessel denoted v_1 at the right of Fig. 13 can be explain by the low curvature of the tangent surface of the other vessel v_2 in the direction orthogonal to v_1. This low curvature, equal to zero here, disturb the medialness response which integrate boundariness along a circle orthogonal to v_1 axis.

In the same way, when a small vessel is tangent to a "bigger" one, we can expect disturbance in the small vessel axis detection due to the low curvature of the big vessel, even when vessels are parallel i.e. for low values of α.

As a conclusion, when the boundaries of tangent vessels are not in contact, one can expect to keep the continuity of the vessels centers. Nevertheless, tangency of vessels have the following negative effects: - it decreases the response function and makes the thresholding more difficult, - it increases the estimated size of the vessel near the tangent area, - it changes the location of centerlines. One way to improve the detection of tangent vessels can be to make an iterative process. The information of the detected vessels can be used to localize the region of tangency and to discard the information of gradient in those regions for the next iteration.

4.1.6 Junctions

A junction in a vessels network is a branching of vessel, where one vessel divides into several branches, in general two. We restrict this experimental study to the case of two branches.

Although the modelization does not include any vessels junction, some of them may be properly detected. Fig. 14 shows experiments made on three synthetic junction images.

The centerlines detection, obtained from the extraction of local maxima of the multiscale response, does not ensure the continuity of the junction detection. In the top image, the main vessel divides into two branches of the same size and the continuity is preserved, but in the middle and in the bottom image, the two branches don't have the same size and the junction continuity is not preserved by the centerlines. This discontinuity can still be present after the reconstruction (middle image).

Disconnection disturbs the interpretation of the reconstruction and the characterization of the vascular tree topology. To solve this problem, the junctions can be connected using the centerlines and the radii information. Assuming that the bigger vessel keeps its continuity, a junction is restored when the distance between extremity E of a vessel v_1 and the axis of second vessel v_2 is lower than the radius of v_2:

$$d(E, v_2) < r(v_2) * \alpha + \beta \tag{16}$$

where α stands for the error in radius estimation and β is the sum of the error in the location of v_2 axis and in the location of the extremity E of v_1. To perform the junction connection, each extremity E of a vessel v_1 is projected on every segment of every vessel different from v_1 and located in the vicinity of E, and d is the distance to the nearest projected point P. We set $\alpha = 1.2$ and $\beta = 2$ voxels. Fig. 14 shows the restored centerlines and the reconstruction from those centerlines for two junction images.

4.2 Image of a phantom

4.2.1 Characteristics of the phantom image

We have a phantom image created by General Electric Medical Systems, on which the sizes of the different structures is known before the acquisition. This image is coded on 2 bytes and its size is $512 \times 512 \times 512$, the voxels are isotropic with a size of 0.267 mm. Fig. 15 shows two Maximum Intensity Projections of this image compared with its map containing real sizes of some structures. This phantom image allows us to estimate the error made in the estimation of the vessel size. The Gaussian blob is not a good model for the section of the vessel and using this model leads to under-estimation of the size of structures. Thus, in the following experiments, we use the relation between the maximal scale and the radius of the structure for the bar-like convolved cross-section model presented in paragraph 4.1.2. This relation is was given in Fig. 8. The standard deviation of the Gaussian convolution is set to $\sigma_p = 1.5$ voxels.

4.2.2 Extraction of tubular structures and size estimation

cylinder LW The size of LW is 2 mm, i.e. 3.744 voxels. From our multiscale analysis with 20 scales for radii ranging from 2 to 6 voxels, we estimated the radius at 3.778 voxels. The corresponding estimated diameter is 2.018 mm.

cylinder E The cylinder named E in Fig. 15 has a size of 4 mm. From our multiscale analysis with 20 scales for radii ranging from 6 to 9 voxels, we estimated the radius at 7.270 or 7.427 voxels along the detected centerline. In fact, the responses for those two successive scales are very close. The corresponding estimated diameters in are 3.884 mm and 3.968 mm.

cylinders LD and SD Fig. 17 shows the results on the structure with varying width: LD=4 mm and SD=2 mm. The multiscale analysis was run on 20 scales ranging from sizes of 3 voxels to 9 voxels. The maximum radius found for LD is 3.6 mm and the minimum radius found for SD is 2.14 mm.

4.3 Real Images

4.3.1 Brain Vessels from X-ray images

Image Acquisition Our algorithm was tested on a set of images produced by General Electric Medical Systems, Buc, France. They are obtained by 3D reconstruction of the vessels from 2D X-ray substracted angiographies. Details of the reconstruction scheme can be found in [Pay96]. Compared to the other 3D acquisition modalities which are Magnetic Resonance Angiography and Scanner Angiography, this 3D reconstruction gives a high isotropic resolution over the whole reconstructed volume. However, it requires a good opacification of the vascular network obtained with an intra-arterial injection. The left images in Fig. 18 are MIP views of a typical sub-images centered on an aneurysm. They contain different artefacts: noise, partial volume effect, consequences of the patient motion between different acquisitions and 3D reconstruction artefacts which lead to a non-homogeneity of the intensity of the vessels for different sizes of the vessel. The two right columns of Fig. 18 show isosurfaces of the images, where small vessels are only visible with a low threshold (surface holes in black are due to the image boundaries).

Choice of parameters We tested our algorithm on ten images $128 \times 128 \times 128$ of varying complexity. Because small vessels have a lower intensity than bigger ones, we used a parameter γ lower than 1 for the normalization. Decreasing the value of γ has the effect of enhancing small vessels compared to big ones, and helps to compensate for intensity variations. We used the value 0.75 for γ. The minimum and maximum scales are chosen according to the radii of the thinnest and the thickest vessels in the initial image. The algorithm was run with then scales that detect vessels of radii ranging from 0.4 to 6 voxels. The computation time for obtained the local maxima image is approximately 15 minutes on a Dec Alpha station 500, running at 400 MHz. Then, after manual thresholding, the centerlines extraction takes a few seconds.

Results Results on the three images of Fig. 18 are shown in Fig. 21. On the left, the detected centerlines are represented with an isosurface of the initial image and using transparency. On the right, a surface of the reconstructed network is represented, the reconstruction is based on the previous centerlines and the estimated radii. The following point are emphasized: *First image*, a separate detection of two tangent vessels. *Second image*, on the left, a continuous detection of a vessel with high curvature; on the right, the detection of a vessel in the vicinity of the aneurysm, the location of this vessel was difficult to understand in both MIPs and isosurfaces. *Third image*, the detection of a vessel with low and decreasing intensity and several well-detected junctions.

4.3.2 Brain MRA

Fig. 22 shows a brain MRA $512 \times 512 \times 60$ with voxel dimensions $0.46875 \times 0.46875 \times 0.7\text{mm}^3$ [1]. From this image we extracted a sub-volume $136 \times 127 \times 60$ shown at the top left of Fig. 23. Compared to previous X-ray images, vessel detection is more difficult because the intensity inside the vessels is less homogeneous, the vessels are not isotropic and noise is more important. A solution to reduce noise and inhomogeneous intensity inside vessels is to apply a pre-filtering method like anisotropic diffusion. Several works have been done on nonlinear diffusion and anisotropic filtering [PM90, AGLM93, tHR94], and also on its application to vessel enhancement [KMA97, OBMC97].

Top right image of Fig. 23 shows the image after anisotropic diffusion where a threshold on the gradient norm is used to control the diffusion.

To deal with non-isotropic voxels, the program adapts the sizes of the Gaussian kernel convolution along x, y and z axis. Voxel dimensions are also used to estimate first and second derivatives in each direction and to convert spatial coordinates into image coordinates when computing the response function.

The bottom left image represents the local extrema extracted from the filtered image and the bottom right image represents a surface rendering of the vessels reconstruction.

5 Conclusion and Discussion

We presented a multiscale approach for tubular structures detection in 3D images. Our approach uses gradient information at a given distance of the vessels centers. Based on different models of vessels, we expressed eigenvectors and eigenvalues of the Hessian matrix and showed their sensitivity to elliptical cross-section, to vessel curvature and to the distance of the point to the real vessel center. Using a cylindrical circular model with Gaussian blob cross-section, we found the optimal distance for computing gradient information at a given scale, and we also expressed the vessel radius as a function of the maximal scale.

Then, we proposed a method for extracting centerlines and reconstructing the whole vessels network. Experiments on synthetic images show the limits and the robustness of the algorithm according to radius variations, to curvature, and to junctions for vessels with Gaussian cross-sections. A bar-like convolved cross-section model was also introduced and we derived a new size estimation for this model with formal calculus simulations. Robustness

[1] The authors thank Marc Thiriet from INRIA Rocquencourt for providing the image

of the size estimation was tested on a phantom image and results were presented on real X-ray and MRA images of brain vessels.

Several conclusions and research directions follow from this work. The first point is the importance of extracting the vessels centerlines, and ensuring their continuity to understand the topology of the vessels network. For this purpose, the variable intensity at the center of vessels of different sizes is still an important issue and has to be taken into account in the vessel model. This can lead for example to a specific response normalization. A second important issue is the discrimination between vessel and non-vessel structures. This discrimination is present in our method at the pre-selection stage based on Hessian matrix eigenvalues and also in the response function that enhances vessel centers. However, another discrimination of the local maxima may be necessary when the image contains non-vessel structures with high gradients or to remove wrong extrema obtained near the vessels frontiers. Finally, once a good detection of the centerlines is obtained, a second and more precise detection of the vessels contours may be done based on this information and without assuming a circular cross-section profile.

A Expression of the maximal scale depending on γ

We want to detect the axis of the vessel which is defined by $x = y = 0$. The response at a point $M(0,0,z)$ is given by:

$$R_t(\bar{x}) = \frac{1}{2\theta\pi\sqrt{t}} \int_{\bar{x}\in C_{\theta\sqrt{t}}} |\nabla L(\bar{x},t).\vec{n}|\, d\bar{x}$$

which corresponds to the mean of the vector product of the gradient with the unit radial vector along the circle of center $(0,0,z)$ and of radius $\theta\sqrt{t}$. The gradient and the normal vector $\vec{n}$ have the following expressions:

$$\nabla L(\bar{x},t) = L(\bar{x},t)\frac{-1}{t+\sigma_0^2}\begin{pmatrix} x \\ y \\ 0 \end{pmatrix}$$

$$\vec{n} = \frac{1}{\sqrt{x^2+y^2}}\begin{pmatrix} x \\ y \\ 0 \end{pmatrix} \text{ with } x^2+y^2 = \theta^2 t$$

then

$$|\nabla L(\bar{x},t).\vec{n}| = C\frac{\theta\sqrt{t}}{2\pi\,(t+\sigma_0^2)^2}\, e^{-\frac{\theta^2 t}{2(t+\sigma_0^2)}}$$

This last expression is no longer a function of $\bar{x}$, then the mean of this expression along the circle is straightforward, and

$$R_t = C\frac{\theta\sqrt{t}}{2\pi\,(t+\sigma_0^2)^2}\, e^{-\frac{\theta^2 t}{2(t+\sigma_0^2)}}$$

The normalized response R_t^n is defined by $R_t^n = t^{\gamma/2} R_t$ and its partial derivative on t is:

$$\frac{\partial R_t^n}{\partial t} = A \frac{C t^{\frac{\gamma-1}{2}}}{4\pi\,(t+\sigma_0^2)^4} e^{-\frac{\theta^2 t}{2(t+\sigma_0^2)}}$$

with $A = (\gamma-3)t^2 + (2\gamma - 2 - \theta^2)\,\sigma_0^2\,t + (1+\gamma)\sigma_0^4$.

We are looking for the value of γ which gives a maximum for the function R_t^n at $t = \sigma_0^2$. Thus we want $\frac{\partial R_t^n}{\partial t}$ to have a positive root which corresponds to a maximum.

The sign of $\frac{\partial R_t^n}{\partial t}$ is the same as the sign of A, and the expression A, when $\gamma < 3$ and the determinant Δ is also positive, has only one positive root which corresponds to a maximum for R_t^n :

$$h(\gamma,\theta) = \frac{\sqrt{\Delta} - 2\gamma + 2 - \theta^2}{2(3-\gamma)}$$

with

$$\Delta = \left[\theta^2 - (2\gamma - 2)\right]^2 + 16 - (2\gamma-2)^2.$$

B Convolved bar-like model

The analytic definition of the model was given by Eq. (15), and is

$$\begin{aligned} I(x,y,z) &= f_r(x,y) * G_{\sigma_p}(x,y) \\ &= \big(f_r(x,y) * G_{\sigma_p}(x)\big) * G_{\sigma_p}(y) \end{aligned}$$

The convolution product can be replaced by integrals, then the integral through x axis is expressed as following:

$$\begin{aligned} f_r(x,y) * G_{\sigma_p}(x) &= \int_{t=-\infty}^{t=+\infty} f_r(x-t,y) G_{\sigma_p}(t) dt \\ &= \int_{t=-x-r_1}^{t=-x+r_1} f_r(x-t,y) G_{\sigma_p}(t) dt \end{aligned}$$

where $r_1 = \sqrt{r^2 - y^2}$

$$\begin{aligned} f_r(x,y) * G_{\sigma_p}(x) &= \int_{t=-x-r_1}^{t=-x+r_1} G_{\sigma_p}(t) dt \\ &= \mathcal{G}_{\sigma_p}(-x + \sqrt{r^2-y^2}) - \mathcal{G}_{\sigma_p}(-x - \sqrt{r^2-y^2}) \\ &= \mathcal{G}_{\sigma_p}(x + \sqrt{r^2-y^2}) - \mathcal{G}_{\sigma_p}(x - \sqrt{r^2-y^2}) \end{aligned}$$

where $\mathcal{G}_{\sigma_p}$ is a primitive of G_{σ_p} chosen to be an odd function.

$$\mathcal{G}_{\sigma_p} = \frac{1}{2}\, erf\left(\frac{x}{\sqrt{2}\sigma_p}\right)$$

where the function erf is defined by:

$$erf(x) = \frac{2}{\sqrt{\pi}} \int_{t=0}^{x} e^{-t^2} dt$$

$$\begin{aligned} I_{\sigma_p}(x,y,z) &= f_r(x,y) * G_{\sigma_p}(x,y) \\ &= \big(f_r(x,y) * G_{\sigma_p}(x)\big) * G_{\sigma_p}(y) \\ &= \int_{-r}^{+r} \left[\mathcal{G}_{\sigma_p}(x+\sqrt{r^2-u^2}) - \mathcal{G}_{\sigma_p}(x-\sqrt{r^2-u^2})\right] G_{\sigma_p}(y-u)du \quad (17) \end{aligned}$$

The derivative of the intensity along x axis can also be expressed analytically, and then the expression of the response at the vessel center and for a scale $t = \sigma^2$ is deduced:

$$\begin{aligned} \frac{\partial I_{\sigma_p}}{\partial x}(x,y,z) &= \int_{-r}^{+r} \left[G_{\sigma_p}(x+\sqrt{r^2-u^2}) - G_{\sigma_p}(x-\sqrt{r^2-u^2})\right] G_{\sigma_p}(y-u)du \\ R_\sigma = \frac{\partial I_\alpha}{\partial x}(\theta\sigma,0,z) &= \int_{-r}^{+r} \left[G_\alpha(\theta\sigma+\sqrt{r^2-u^2}) - G_\alpha(\theta\sigma-\sqrt{r^2-u^2})\right] G_\alpha(-u)du \quad (18) \end{aligned}$$

with $\alpha = \sqrt{\sigma_p^2 + \sigma^2}$.

References

[AGLM93] L. Alvarez, F. Guichard, P.L. Lions, and J.M. Morel. Axioms and fundamental equations of image processing. *Archive for Rational Mechanics*, 123(3):199–257, September 1993.

[Blu67] H. Blum. A transformation for extracting new descriptors of shape. In W. Wathe-Dunn, editor, *Models for the perception of Speech and Visual Form*, pages 363–380, MIT Press, Cambridge, 1967.

[BM94] G. Bertrand and G. Malandain. A new characterization of three-dimensional simple points. *Pattern Recognition Letters*, 15(2):169–175, February 1994.

[BN78] H. Blum and R.N. Nagel. Shape description using weighted symmetric axis features. *Pattern Recognition*, 10:167–180, 1978.

[Del94] H. Delingette. Intrinsic stabilizers of planar curves. In *3rd European Conference on Computer Vision (ECCV'94)*, Stockholm, Sweden, June 1994.

[EGMP94] D. Eberly, R. Gardner, B. Morse, S. Pizer, and C. Scharlach. Ridges for image analysis. *Journal of Mathematical Imaging and Vision*, 4:353–373, 1994.

[FEPM95] D. S. Fritsch, D. Eberly, S. M. Pizer, and M. J. McAuliffe. Simulated cores and their application in medical imaging. *Information Processing in Medical Imaging*, 365–368, 1995.

[Fid97] Márta Fidrich. Following feature lines across scale. In *Scale-Space Theory in Computer Vision*, pages 140–151, Springer-Verlag, Utrecht, July 1997.

[FKMP97] J.D. Furst, R.S. Keller, J.E. Miller, and S.M. Pizer. Image loci are ridges in geometric spaces. In *First Intern Conf on Scale-Space Theory in Computer Vision*, Utrecht, July 1997.

[FP98] J.D. Furst and S.M. Pizer. *Marching Optimal-Parameter Ridges: an Algorithm to Extract Shape Loci in 3D Images.* Technical Report TR-98-006, University of North Carolina, 1998.

[FPE96] J.D. Furst, S.M. Pizer, and D. Eberly. Marching cores: a method for extracting cores from 3d medical images. In *Proc. Workshop on Math. Methods in Biomed. Image Anal.*, pages 124–130, IEEE, 1996.

[FPME94] D.S. Fritsch, S. M. Pizer, B. S. Morse, D.H. Eberly, and A. Liu. The multiscale medial axis and its applications in image registration. *Pattern Recognition Letters*, 15(5):445–452, 1994.

[Fra98] F. Frangi. Multiscale vessel enhancement filtering. In W. M. Wells, A. Colchester, and S. Delp, editors, *Medical Image Computing and Computer-Assisted Intervention (MICCAI'98)*, pages 130–137, Springer, October 1998.

[FtHRKM92] L.M. Florack, B.M. ter Haar Romeny, J.J. Koenderink, and Viergever M.A. Scale and the differential structure of images. *Image and Vision Computing*, 10(6):376–388, July 1992.

[KGSD95] T.M. Koller, G. Gerig, G. Székely, and D. Dettwiler. Multiscale detection of curvilinear structures in 2D and 3D image data. In IEEE, editor, *International Conference on Conputer Vision (ICCV'95)*, pages 864–869, 1995.

[KMA97] K. Krissian, G. Malandain, and N. Ayache. Directional anisotropic diffusion applied to segmentation of vessels in 3d images. In *Scale-Space Theory in Computer Vision (Scale-Space'97)*, pages 345–348, Utrecht, The Netherlands, July 1997. Springer, LNCS 1252.

[KMA98] K. Krissian, G. Malandain, and N. Ayache. *Model Based Multiscale Detection and Reconstruction of 3D Vessels.* Technical Report 3442, INRIA Sophia Antipolis, 2004 route des Lucioles BP 93 06902 Sophia Antipolis Cedex (France), June 1998.

[KMAV98a] K. Krissian, G Malandain, N. Ayache, R. Vaillant, and Y. Trousset. Model-based multiscale detection of 3d vessels. In *Computer Vision and Pattern Recognition*, pages 722–727, June 1998.

[KMAV98b] K. Krissian, G Malandain, N. Ayache, R. Vaillant, and Y. Trousset. Model-based multiscale detection of 3d vessels. In Baba Vemuri, editor, *Workshop on Biomedical Image Analysis*, pages 202–208, Santa Barbara, 1998.

[Koe84] J. J. Koenderink. The structure of images. *Biol. Cybern.*, 50(363-370), 1984.

[LC87] W.E. Lorensen and H.E. Cline. Marching cubes: A high resolution 3-D surface construction algorithm. *Computer Graphics*, 21(4):163–169, 1987.

[LCBF97] C. Lorenz, I.-C. Carsen, T.M. Buzug, C. Fassnacht, and J. Weese. Multi-scale line segmentation with automatic estimation of width, contrast and tangential direction in 2d and 3d medical images. In *CVRMed-MRCAS'97*, pages 213–222, Grenoble, France, March 1997. Lecture notes in Computer Science 1205, Springer Verlag.

[Lin94] T. Lindeberg. *Scale-Space Theory in Computer Vision.* Kluwer Academic Publishers, Dordrecht, Netherlands, 1994.

[Lin96] T. Lindeberg. Edge detection and ridge detection with automatic scale selection. In *IEEE Comp. Soc. Conf. on Computer Vision and Pattern Recognition*, page 465, San Francisco, June 1996.

[MPL94] B.S. Morse, S.M. Pizer, and A. Liu. Multiscale medial analysis of medical images. *Image and Vision Computing Volume*, 12(6):327–338, July/August 1994.

[OBMC97] M.M. Orkisz, C. Bresson, I.E. Magnin, O. Champin, and P.C. Douek. Improved vessel visualization in mr angiography by nonlinear ansiotropic filtering. *Magnetic Resonance in Medicine*, 37(6):914–919, June 1997.

[Pay96] Etienne Payot. *Reconstruction Vasculaire tridimensionnelle en imagerie par rayons X.* Ph.D. dissertation, Ecole Nationale Supérieure des Télécommunication, 1996.

[PBCF94] S.M. Pizer, C.A. Burbeck, J.M. Coggins, D.S. Fritsch, and B.S. Morse. Object shaphe before boundary shape: Scale-space medial axes. *Journal of Mathematical Imaging and Vision*, 4:303–313, 1994.

[PEFM98] S.M. Pizer, D. Eberly, D. Fritsch, and B.S. Morse. Zoom-invariant vision of figural shape: The mathematics of cores. *Computer Vision and Image Understanding*, 69(1):55–71, January 1998.

[PM90] P. Perona and J. Malik. Scale-Space and edge detection using anisotropic diffusion. *IEEE Transactions on Pattern Analysis and Machine Intelligence*, 12(7):629–639, July 1990.

[SNAK97] Y. Sato, S. Nakajima, H. Atsumi, T. Koller, G. Gerig, S. Yoshida, and R. Kikinis. 3d multi-scale line filter for segmentation and visualization of curvilinear structures in medical images. In *CVRMed-MRCAS'97*, pages 213–222, March 1997. Lecture Notes in Computer Science 1205, Springer Verlag.

[SNSA98] Y. Sato, S. Nakajima, N. Shiraga, H. Atsumi, S. Yoshida, T. Koller, G. Gerig, and R. Kikinis. Three-dimensional multi-scale line filter for segmentation and visualization of curvilinear strutures in medical images. *Medical Image Analysis*, 2(2):143–168, June 1998.

[TG92] J.P. Thirion and A. Gourdon. *The 3D marching lines algorithm and its application to crest lines extraction.* Technical Report RR-1672, INRIA, Sophia-Antipolis, 1992.

[TG93] J.P. Thirion and A. Gourdon. *The marching lines algorithm:New results and proofs.* Technical Report RR-1881-1, INRIA, Sophia-Antipolis, 1993.

[tHR94] B.M. ter Haar Romeny, editor. *Geometry-Driven Diffusion in Computer Vision.* Kluwer Academic Publishers, Dordrecht, 1994.

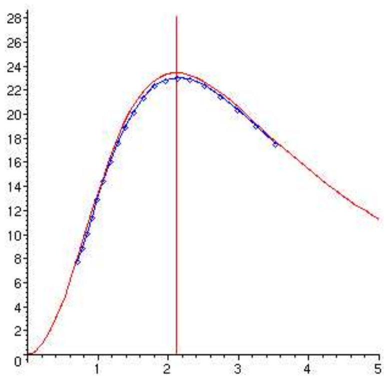

Figure 3: Response obtained at the center of the vessel for different scales. In red, the theoretical profile, and in blue the obtained profile. The vertical line shows the theoretical scale for which the response is maximal.

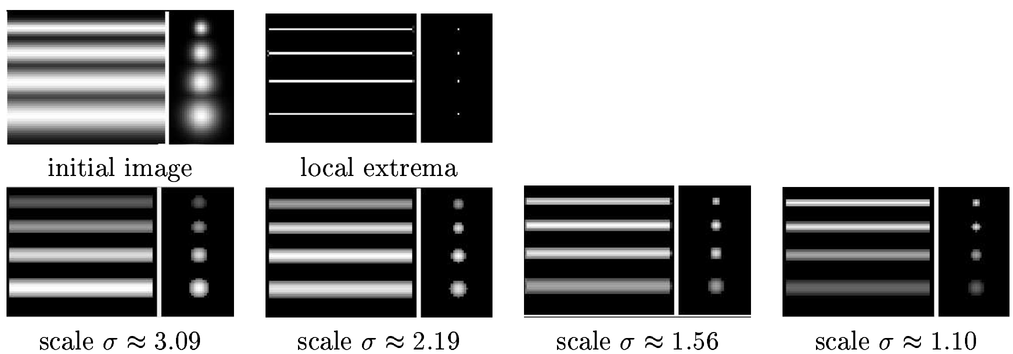

Figure 4: cylinder with circular Gaussian cross-section. Responses obtained for the optimal scales.

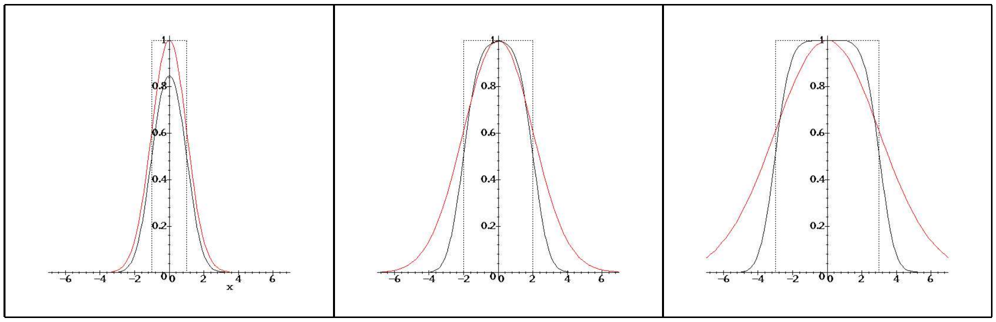

Figure 5: Ilustration of the 1D bar-like convolved model. From left to right: models for a 1D vessel with radius 1,2 and 3. In red, a normalized Gaussian model. In black, convolution of a bar-like model with a Gaussian of standard deviation 0.7.

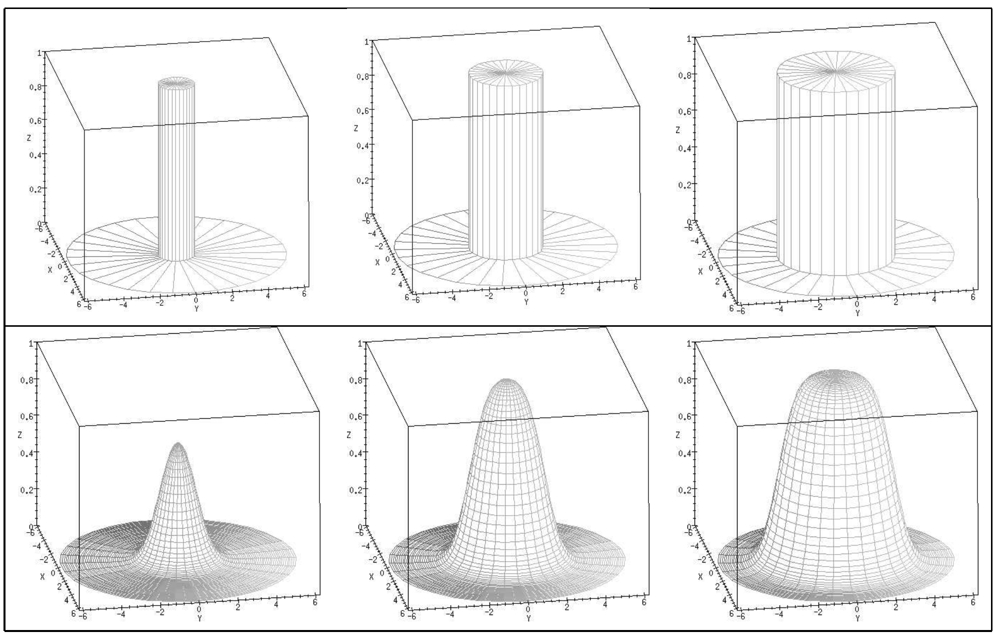

Figure 6: Ilustration of the cross-section of the 3D bar-like convolved model. At the top, representation of the bar-like cross-section with radii equal to 1, 2 and 3 from left to right. At the bottom, the same cross-sections after convolution with a 2D Gaussian of standard deviation 0.7.

Real vessel radius	1.25	1.75	2.5	3.5
Maximal reponse	20.8085	22.3763	22.7294	22.9052
Difference to the expected value	10.8667%	4.1510%	2.6385%	1.8855%
Estimated radius	1.55	1.79	2.58	3.46
Error in voxels	0.3	0.04	0.08	0.04

Table 3: intensity obtained at the center of the vessels for a range of 10 scales, estimated sizes and error in the estimation. The theoretical expected maximal response is 23.3.

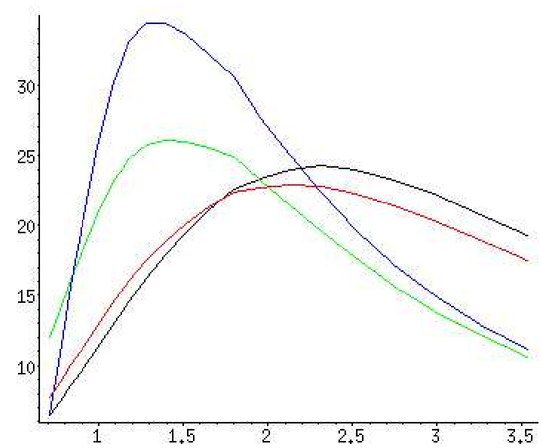

Figure 7: Response profiles obtained for a Gaussian-like cross-section in red, for a bar-like cross-section in blue, for a bar-like cross-section convolved with a Gaussian $\sigma_p = 1$ in green, for a bar-like cross-section convolved with a Gaussian $\sigma_p = 3$ in black.

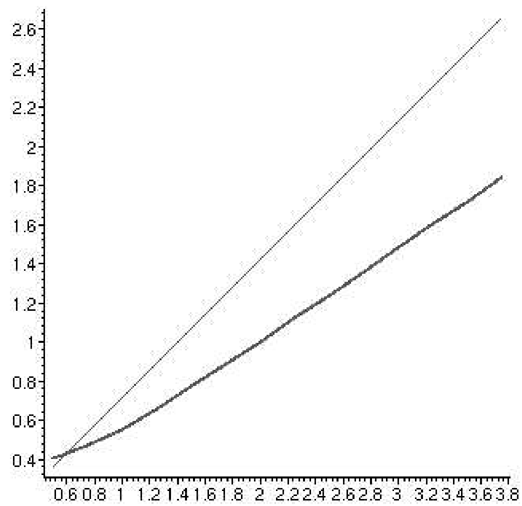

Figure 8:

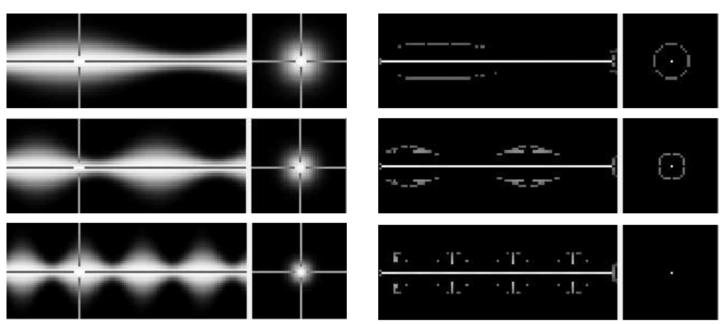

synthetic images local extrema

Figure 9: Tests on an Gaussian cross-section vessel with varying radius.

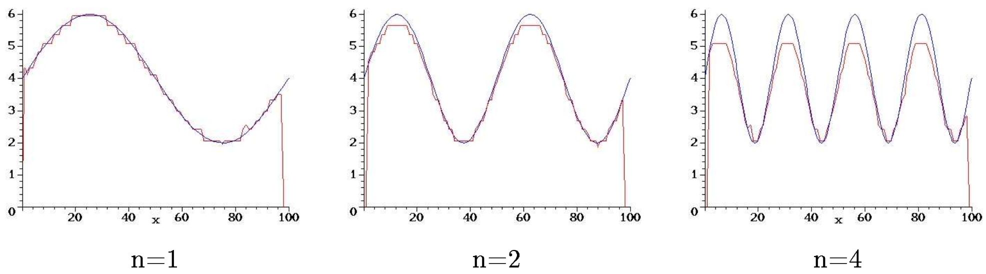

Figure 10: Comparison of the real and the detected radii along z axis.

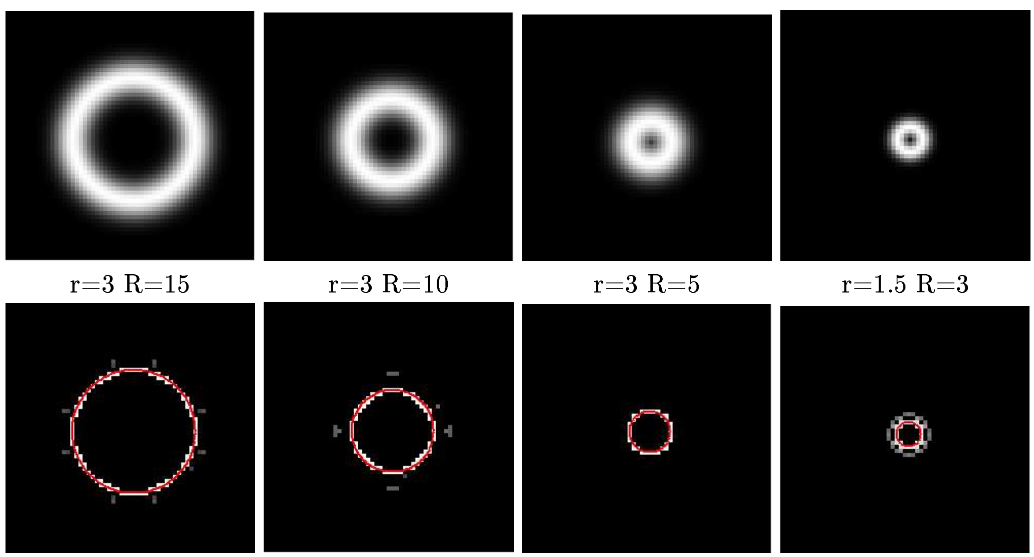

Figure 11: Detection of torus with Gaussian cross-section and different curvatures. At the top, MIPs of the initial images; At the bottom, superimposition of the real torus center (in red) on the local maxima image.

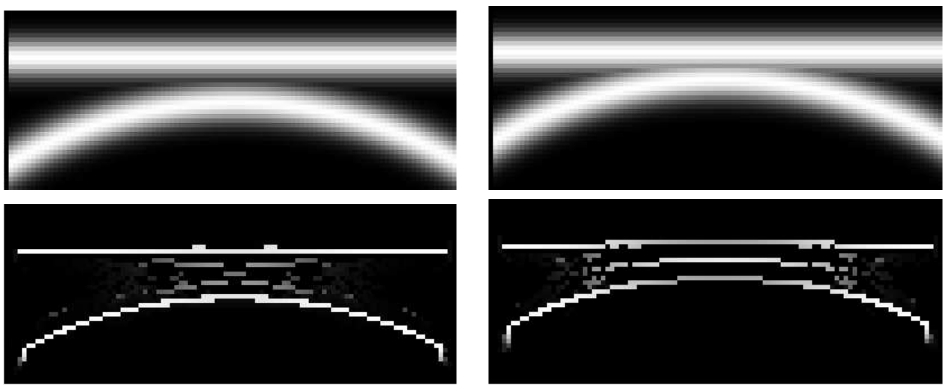

$d = 3$ voxels $d = 0$

Figure 12: Tangent vessel, tangency parallel to the vessel axis ($\alpha = 0$).

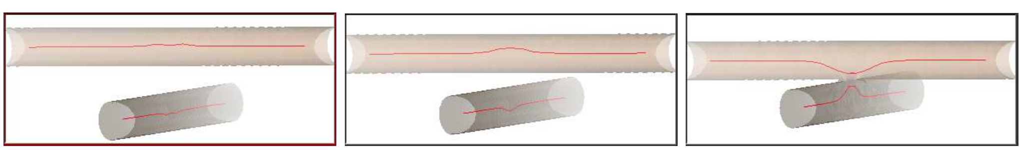

$d = 4$ voxels $d = 2$ voxels $d = 0$

Figure 13: Tangent vessels, tangency orthogonal to the vessel axis ($\alpha = \pi/2$).

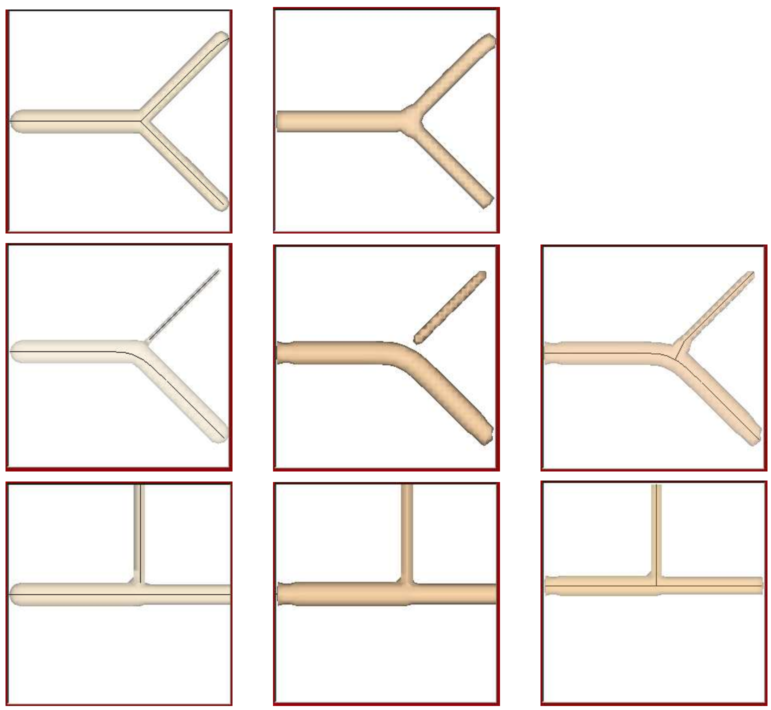

Figure 14: Centerlines detection and reconstruction on three synthetic junction images. Left, initial image and the detected centerlines. Middle, reconstruction before junction connection. Right, centerlines and reconstruction after junction connection.

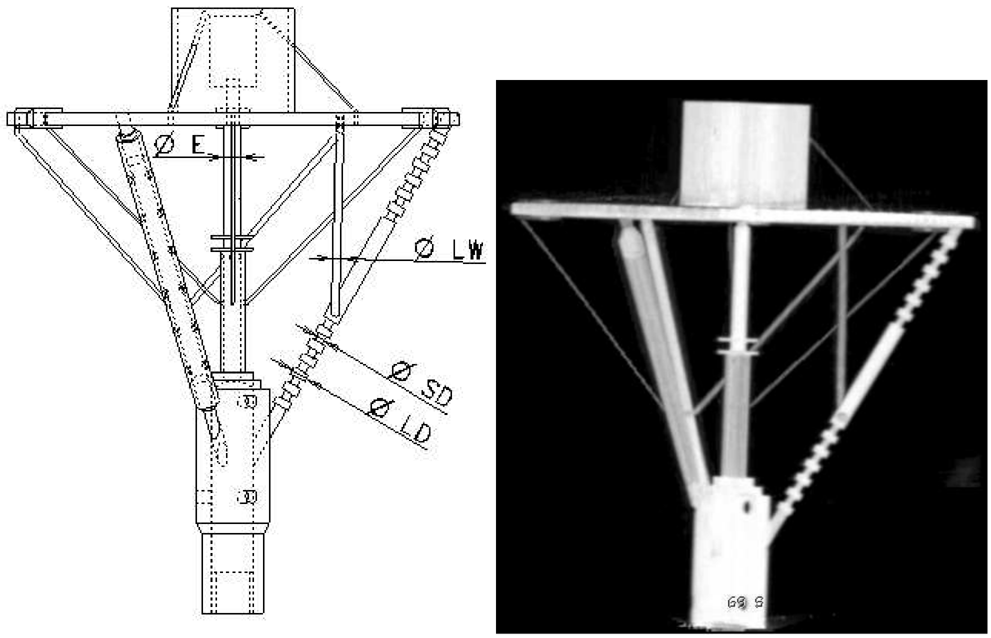

$E = LD = 4\,\mathrm{mm}$, $LW = SD = 2\,\mathrm{mm}$

Figure 15: Phantom image. Left, map of the phantom with the known structures radii. Right, MIP view of the phantom image.

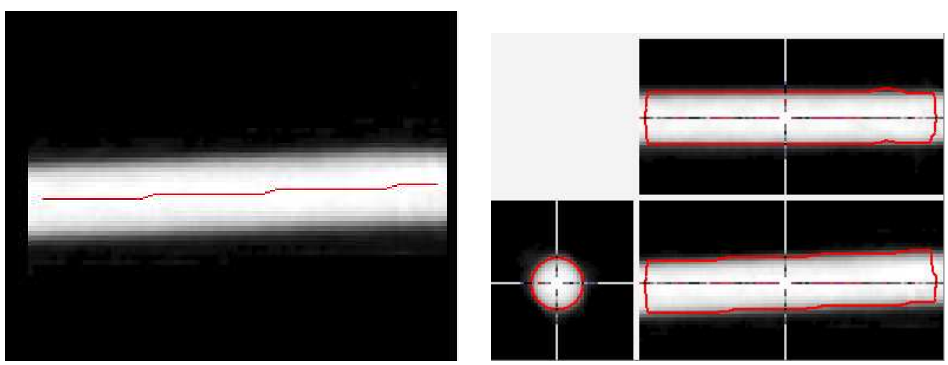

obtained centerline in red. estimated contours of the vessel.

Figure 16: Results on a sub-image of the phantom centered on the diameter E (see figure 15).

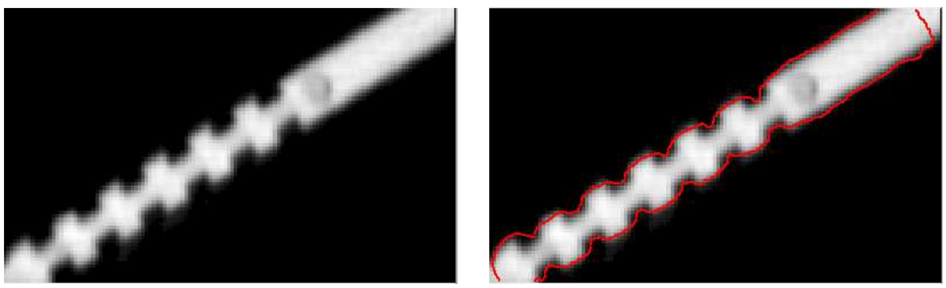

sub-image extracted $127 \times 77 \times 60$ contours of the reconstructed image

Figure 17: Results on a sub-image of the phantom for the diameter SD and LD.

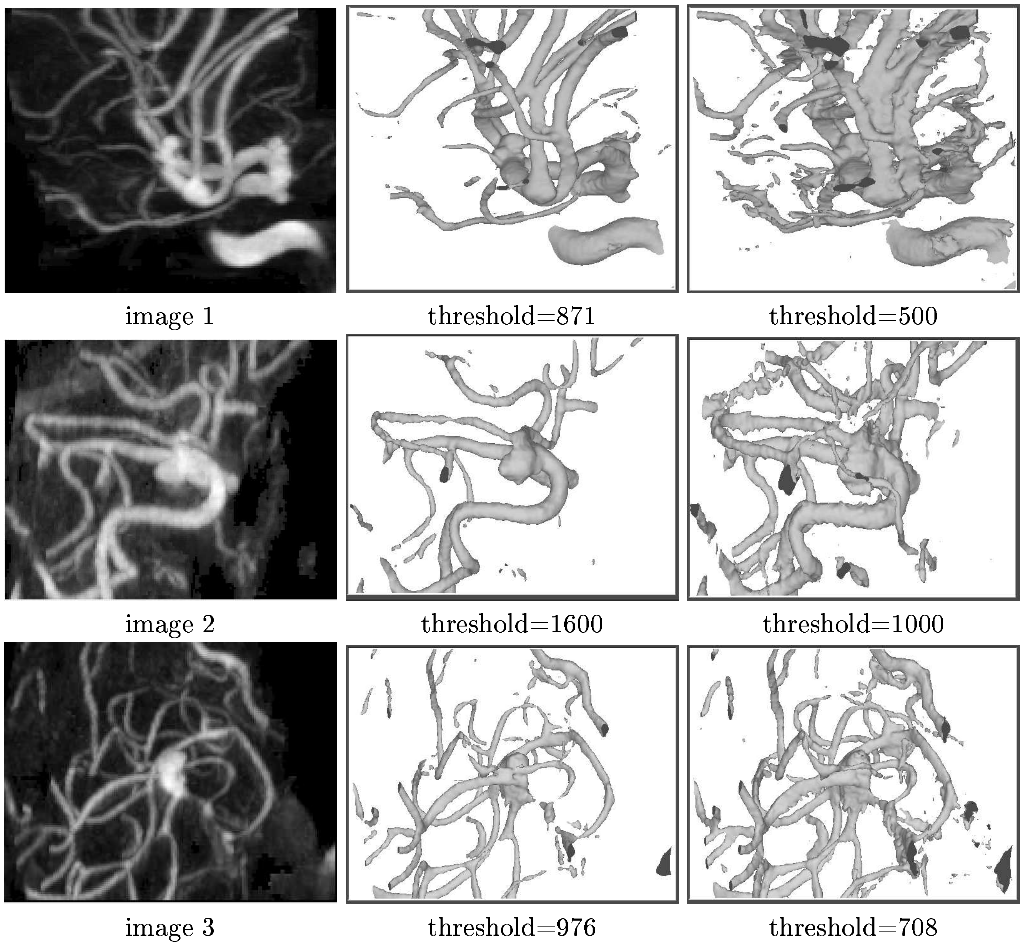

Figure 18: Top, MIP view and isosurfaces of three X-ray 3D images.

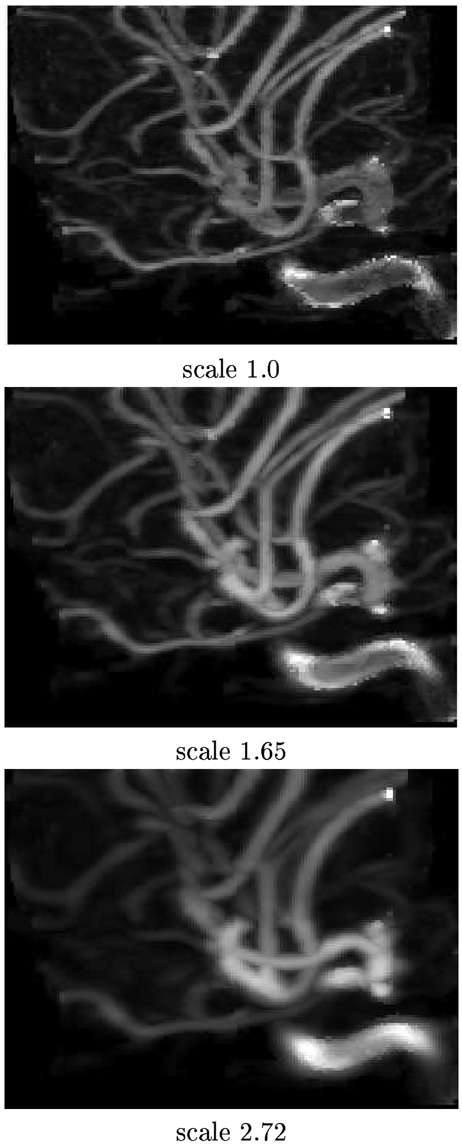

Figure 19: MIP views (Maximum Intensity Projections) of the responses obtained for 6 differents scales.

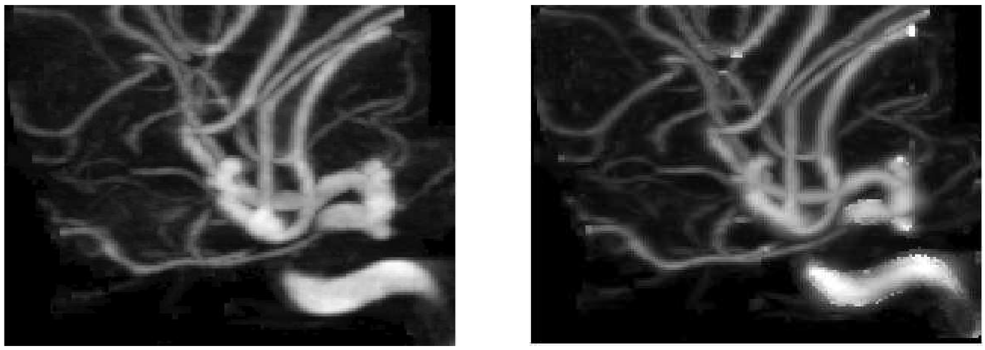

initial image

maximum response across scales

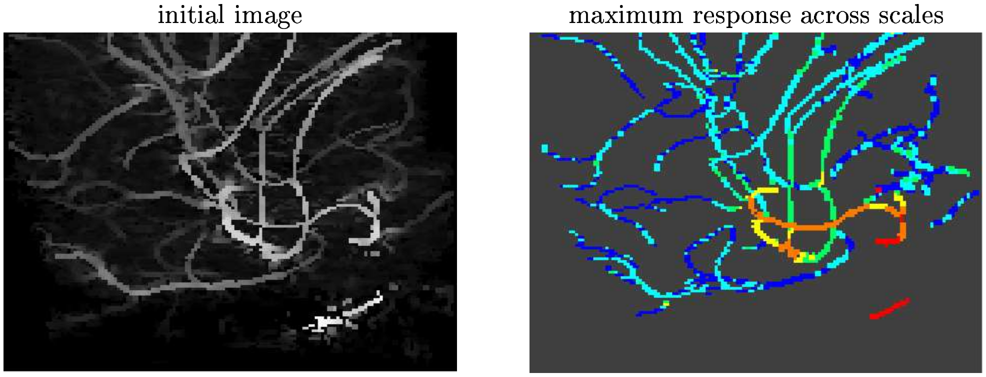

local extrema from the maximum response

center of the vessels with colors depending on the detected scale.

Color						
Scale	1.0	1.28	1.65	2.12	2.72	3.5

Figure 20: MIP views at different stages of the multiscale analysis.

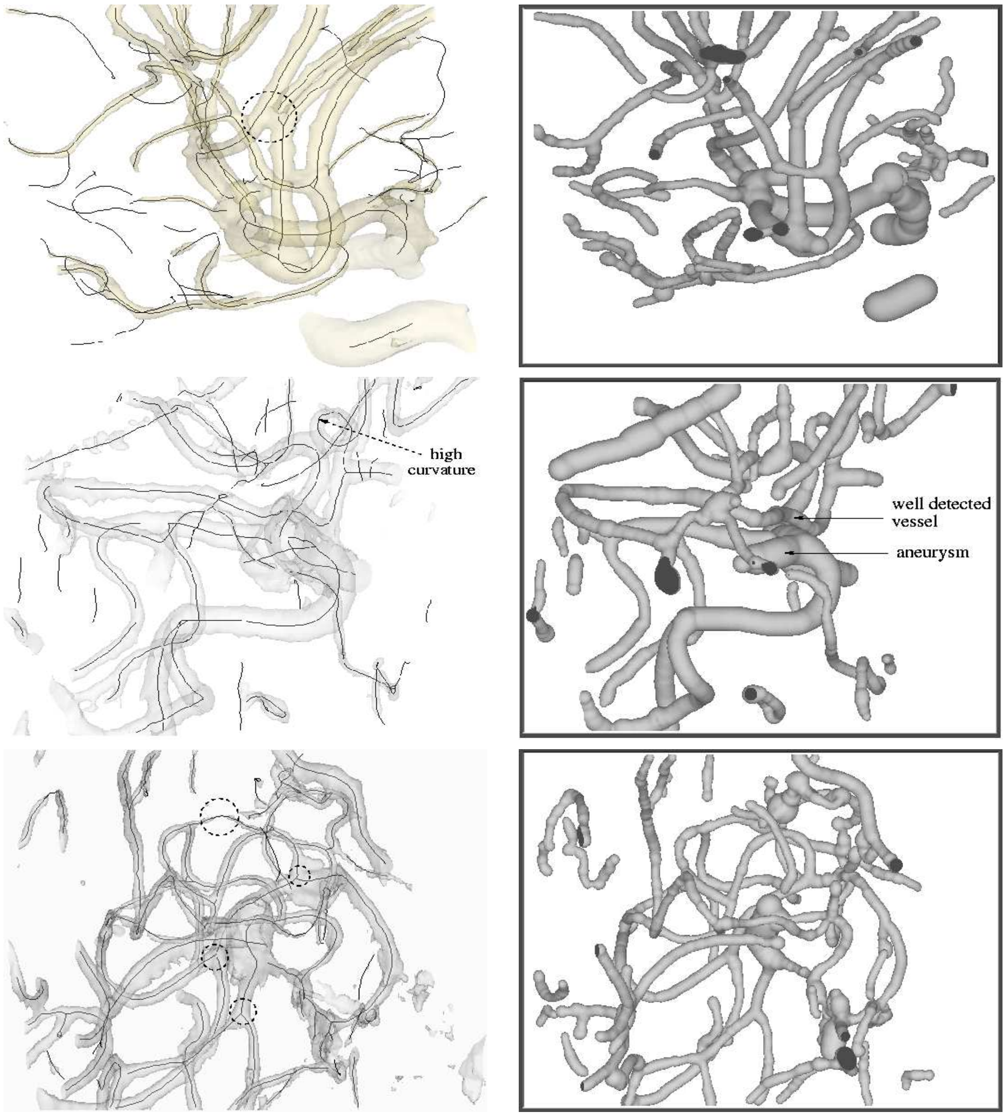

Figure 21: Results on the images represented in Fig. 18. Left, detected centerlines superimposed on an isosurface of the initial image. Right, reconstruction of the vessels network from centerlines and radii estimation.

Figure 22: Initial MRA Image.

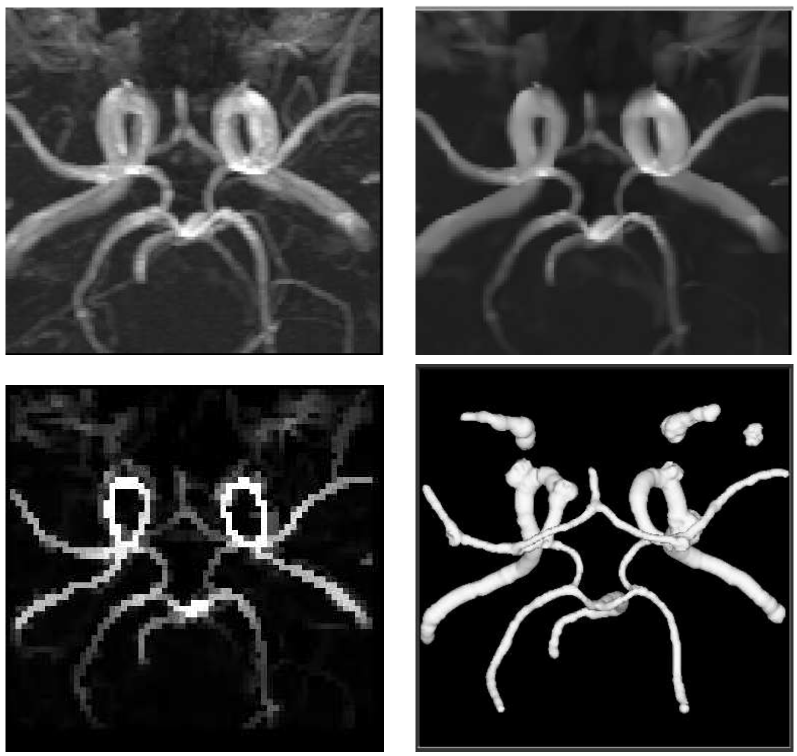

Figure 23: MIP of a sub-image on the top left and the resulting image after anisotropic filtering on the top right. Bottom left, image of the local extrema; and bottom right, vessels reconstruction.

Unité de recherche INRIA Sophia Antipolis
2004, route des Lucioles - B.P. 93 - 06902 Sophia Antipolis Cedex (France)

Unité de recherche INRIA Lorraine : Technopôle de Nancy-Brabois - Campus scientifique
615, rue du Jardin Botanique - B.P. 101 - 54602 Villers lès Nancy Cedex (France)
Unité de recherche INRIA Rennes : IRISA, Campus universitaire de Beaulieu - 35042 Rennes Cedex (France)
Unité de recherche INRIA Rhône-Alpes : 655, avenue de l'Europe - 38330 Montbonnot St Martin (France)
Unité de recherche INRIA Rocquencourt : Domaine de Voluceau - Rocquencourt - B.P. 105 - 78153 Le Chesnay Cedex (France)

Éditeur
INRIA - Domaine de Voluceau - Rocquencourt, B.P. 105 - 78153 Le Chesnay Cedex (France)
http://www.inria.fr
ISSN 0249-6399